



universität
wien

MASTERARBEIT

Titel der Masterarbeit

„Laser-Induced Effects on Single-Layer Graphene“

Verfasser

Rasim Mirzayev

angestrebter akademischer Grad

Master of Science (MSc)

Wien, 2014

Studienkennzahl lt. Studienblatt: A 066 876

Studienrichtung lt. Studienblatt: Masterstudium Physik

Betreuer: Univ. -Prof. Dipl. -Phys. Dr. Jannik C. Meyer

Contents

| | |
|---|-----------|
| 1. Introduction..... | 5 |
| 2. Theory..... | 7 |
| 2.1. Graphene..... | 7 |
| 2.1.1. Basic properties of graphene..... | 7 |
| 2.1.2. Electronic band structure of graphene..... | 9 |
| 2.2. Raman scattering..... | 11 |
| 2.2.1. Phonons..... | 11 |
| 2.2.2. Phonon dispersion in graphene..... | 11 |
| 2.2.3. Theory of Raman scattering..... | 13 |
| 2.2.4. Raman Spectroscopy of Single-Layer Graphene..... | 15 |
| 2.2.5. Defect Characterization by using Raman Spectroscopy..... | 19 |
| 2.2.6. Doping in Graphene..... | 21 |
| 3. Experimental Methods..... | 23 |
| 3.1. Samples..... | 23 |
| 3.2. Raman Spectrometer..... | 24 |
| 3.3. Pulsed Laser..... | 26 |
| 3.4. AFM measurements..... | 26 |
| 4. Results and Discussion..... | 28 |
| 4.1 Laser Exposure and Raman Spectrum..... | 28 |
| 4.1.1. Overview of the Raman Spectrum..... | 28 |
| 4.1.2 Raman mapping measurements..... | 49 |
| 4.1.3 AFM..... | 52 |
| 4.2 Pulsed Laser Experiment..... | 57 |

| | |
|---------------------------------------|-----------|
| 5. Conclusion and Outlook..... | 63 |
| 6. Zusammenfassung..... | 66 |
| Appendix..... | 69 |
| Acknowledgment..... | 73 |
| Bibliography..... | 74 |

Chapter 1

Introduction

Graphene, a two-dimensional sheet of sp^2 hybridized carbon atoms, is often called a "wonder material" due to its unique and extraordinary electronic, thermal and optical properties [1-4]. As a material of great promise in a wide range of areas, graphene has attracted intense research efforts from both academic and industrial communities during the last decade. Graphene is the thinnest material in the world and this thinnest material is stronger than diamond, more conductive than copper and more flexible than rubber. Graphene attracted a strong attention in the field of quantum physics by its anomalous quantum behavior at room temperature such as Klein Tunneling, relativistic quantum Brownian motion, and the Quantum Hall Effect [5-8]. It has a very high charge carrier mobility of $200\,000\text{ cm}^2/\text{Vs}$ [9]. It is a perfect thermal conductor [10] with a very high mechanical strength exceeding 100 GPa [11]. Graphene is also described as the basic building block of all other carbon allotropes such as buckyballs, carbon nanotubes and graphite [12].

Characterization of unique properties of graphene materials often depends on beam techniques with energetic particles such as Raman spectroscopy, scanning electron microscopy (SEM), transmission electron microscopy (TEM), atomic force microscopy (AFM), and x-ray photoelectron spectroscopy (XPS) [13]. One of the most widely used characterization methods is Raman spectroscopy which is a versatile tool for identification and determination of the number of layers in graphene, structural disorder, doping and strain [14].

It has been previously shown that carbon nanostructures and monolayer graphene is sensitive to energetic particles irradiation and can form structural defects and morphological deformations as a result of these processes [15-19]. Despite its practical importance, only a few experimental studies have been conducted related with the potential effects of the laser irradiation on single-layer graphene and it is still not very clear how the laser may affect the properties of graphene and how does the substrate, surrounding environment affect this interaction. Therefore, more investigation is needed to understand the laser-induced effects on graphene.

In this work we investigate the laser-induced effects on single-layer graphene and aim to understand the mechanism behind these effects by employing the Raman spectroscopy and non-contact Atomic Force Microscopy.

Chapter 2

Theory

In this chapter some basic theoretical concepts and models are introduced in order to make the explanations in the next chapters understandable.

2.1 Graphene

2.1.1. Basic Properties of Graphene

Graphene is the name given to a single layer of sp^2 -hybridized carbon atoms which are arranged in a quasi-two-dimensional honeycomb lattice.

Before its discovery in 2004 [20], graphene was not considered to exist in its free form because two dimensional systems were known to be thermodynamically unstable at finite temperatures [21,22]. However, because of the out-of-plane deformations observed in freely suspended graphene sheets as illustrated in Fig.2.1, the existence of graphene does not contradict with this theory [23].

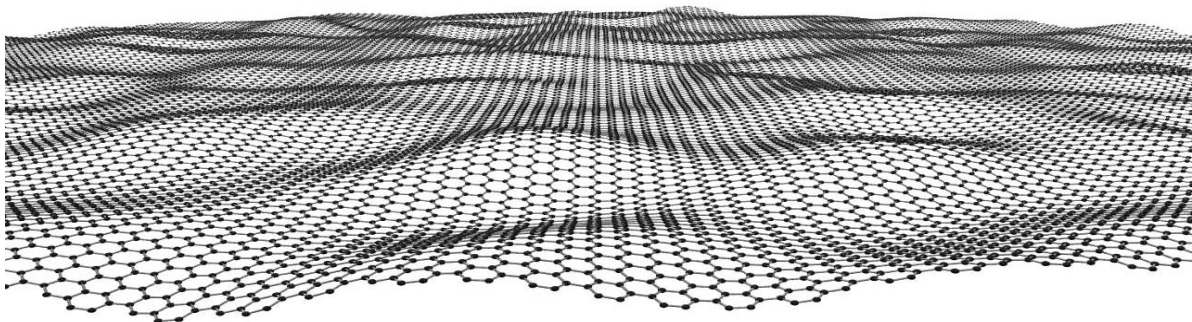


Fig.2.1: Illustration of out-of-plane corrugations in a single-layer graphene sheet. (adapted from Reference [23])

Carbon atoms in graphene are arranged in a trigonal planar geometry which results in a hexagonal honeycomb lattice. The lattice structure can be considered as two equivalent hexagonal sublattices A and B with inversion symmetry. Figure 2.2a. illustrates the lattice structure of graphene and its two sublattices A and B.

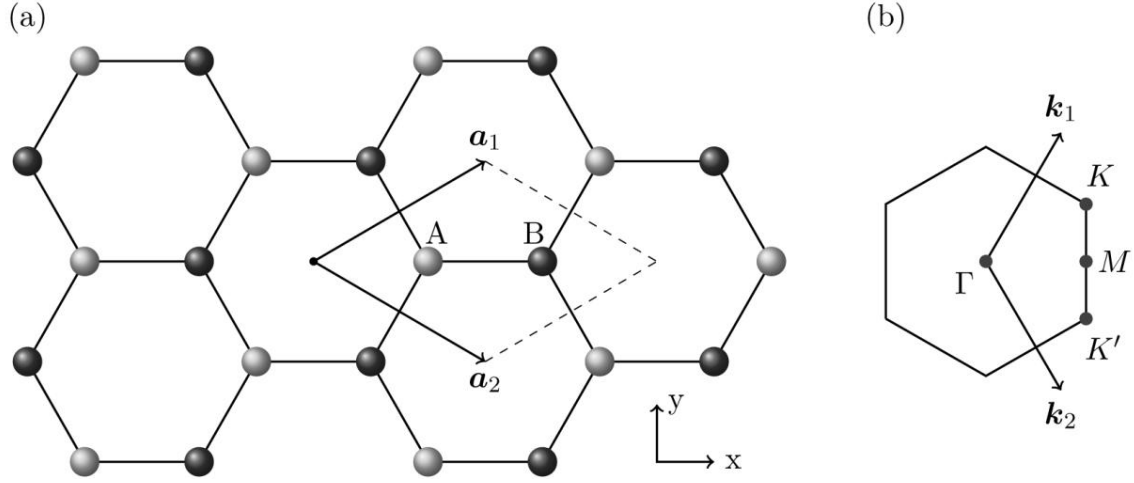


Fig. 2.2.(a) Hexagonal lattice structure of graphene, made out of two interpenetrating lattices (grey and light grey). \mathbf{a}_1 and \mathbf{a}_2 are the unit cell vectors, the dashed line indicates the unit cell. (b) First Brillouin zone of graphene lattice. Γ , K , K' and M are the high symmetry points. (taken from Ref. [24]).

The unit cell in graphene is defined by the two unit cell vectors \mathbf{a}_1 and \mathbf{a}_2 , which are defined as

$$\mathbf{a}_1 = \frac{a}{2} (3, \sqrt{3}) \quad ,$$

$$\mathbf{a}_2 = \frac{a}{2} (3, -\sqrt{3}) \quad ,$$

where $a \approx 0.142$ nm is the carbon-carbon bond length. The lattice constant is given by

$$|\mathbf{a}_1| = |\mathbf{a}_2| = a_0 = \sqrt{3}a \approx 0.246 \text{ nm}$$

The thickness (\mathbf{d}) of single layer graphene sheet is estimated by half of the out-of-plane lattice constant of graphite which is $\mathbf{c} = 2\mathbf{d} = 0.670$ nm [25, 26].

The reciprocal lattice, which is defined as the Fourier transform of the real lattice, is spanned by the vectors \mathbf{k}_1 and \mathbf{k}_2 (see Fig. 2.2(b)).

$$\mathbf{k}_1 = \frac{4\pi}{\sqrt{3}a_0} (0, 1) \quad , \quad \mathbf{k}_2 = \frac{4\pi}{2\sqrt{3}a_0} (\sqrt{3}, -1)$$

Figure 2.2.(b) represents the first Brillouin zone in the reciprocal space with its high symmetry points at the central point Γ , at the two inequivalent corners K and K' and at the M point in between K and K' .

2.1.2 Electronic Band Structure of Graphene

The unique properties of graphene stem from its chemical bonding and crystal structure. Each carbon atom in graphene undergoes an sp^2 hybridization of valence electrons such that one $2s$ orbital is hybridized with the $2p_x$ and $2p_y$ orbitals. These hybridized orbitals form strong σ -bonds between the three nearest neighboring carbon atoms within the plane. The σ -bonds with a carbon-carbon bond length of 0.142 nm are responsible for the mechanical strength of graphene [27]. It has been experimentally proven that graphene is the strongest material ever measured with a Young's modulus of about 1.00 TPa. [11,28]. The remaining valence electrons in the unhybridized $2p_z$ orbitals can bind covalently to neighboring atoms, leading to the formation of half filled, conducting π -bands [29]. The $2p_z$ orbitals are oriented perpendicular to the sp^2 plane and are rotational symmetric around the z-axis. The electrons in the π bands are delocalized and can move freely over the whole structure. The π electrons are primarily responsible for the electronic band structure of graphene at low energies.

The electronic band structure of graphene was first derived in 1947 by Wallace within the tight-binding-model which involves only the interaction between the certain amount of nearest neighbors to an atom [30]. This method employs the Bloch wave functions as linear combinations of the atomic wave functions and neglects the overlapping between the $2p_z$ wave functions of different atoms. Here, the derivation of the electronic band structure is not discussed, however for the detailed derivation the interested reader may refer to References [27,31].

The electronic band structure for π -bonding and π^* -antibonding bands by involving the third-nearest-neighbors is given by (17)

$$E^\pm(\mathbf{k}) = \frac{\varepsilon_{2p} \mp \gamma_0 \sqrt{f(\mathbf{k})}}{1 \mp s_0 \sqrt{f(\mathbf{k})}}, \quad (2.1)$$

where the function $f(\mathbf{k})$ is defined as

$$f(\mathbf{k}) = 3 + 2 \cos 2 \pi a k_1 + 2 \cos 2 \pi a k_2 + 2 \cos 2 \pi a (k_1 - k_2)$$

Here k_1 and k_2 are the components of a wave vector \mathbf{k} in units of the reciprocal lattice vectors \mathbf{k}_1 and \mathbf{k}_2 . Furthermore, ε_{2p} is the matrix element of the Hamiltonian H of the corresponding Schrödinger equation for the Bloch function ϕ_A of atom A, γ_0 is the interaction energy between two carbon atoms and s_0 is the overlap integral between the Bloch functions of atoms A and B. These three parameters can be obtained by fitting experimental data such as ARPES (angle resolved photoemission spectroscopy) data [32]. Figure 2.3 depicts the resulting electronic band structure of single layer graphene. The valence (π) band and conduction π^* bands touch each other at the six corners of the first Brillouin zone. These six points are referred to as \mathbf{K} and \mathbf{K}' points or Dirac cones and lie at the Fermi level. As it is shown in the magnified image in Fig. 2.3, the dispersion relation is linear around the Dirac points and there is no band gap. Due to this unusual and unique band structure, the charge carriers in graphene are regarded as "Massless Dirac Fermions" in analogy to relativistic massless particles like photons with zero effective mass from Dirac theory [1,33]. Consequently, graphene is termed as a "zero-band gap semiconductor or semimetal" in which Dirac equation governs the charge carrier behavior near the Dirac cones at low energies [12].

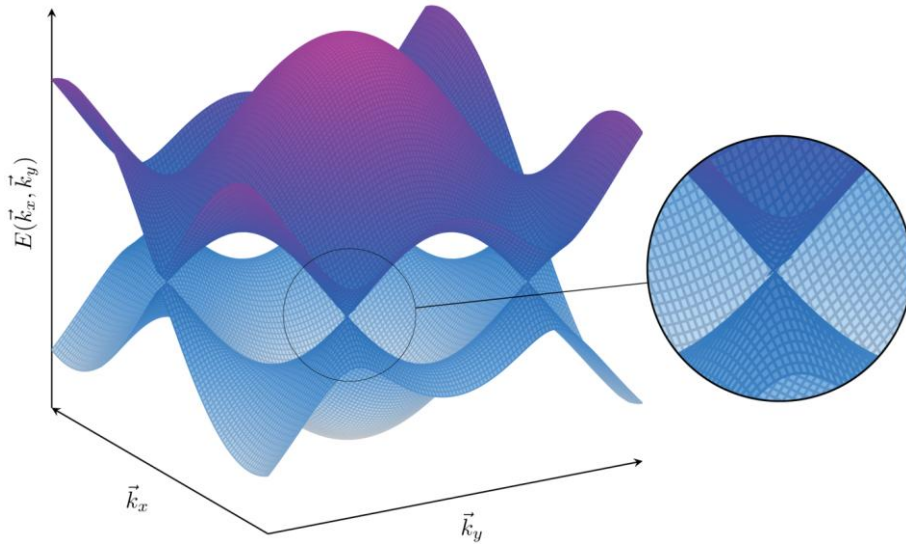


Figure 2.3. The electronic band structure of monolayer graphene obtained within the tight-binding-approximation. The parameters are $\varepsilon_{2p} = 0$, $\gamma_0 = -1.86\text{eV}$ and $s_0 = 0.02$. The zoomed image on the right illustrates the linear dispersion of electronic bands at K point. (adapted with permission of Ref. [24]).

2.2 Raman Scattering

2.2.1. Phonons

The small periodic displacement of an atom from its equilibrium position is defined as atomic vibration. The energy of the vibration motion is transferred to the neighboring atoms. This phenomena can be described by a travelling wave and is referred to as a *phonon*. In other words, from the classical point of view, phonons are the "*vibrations of the lattice*". In the wave-particle duality description of quantum mechanics, phonons are described as quasiparticles representing the quantization of the modes of lattice vibrations. Like photons, phonons are bosons and are characterized by a wave vector \mathbf{k} and an angular frequency ω , with an energy of $E = \hbar\omega$ [34]. The relationship between frequency and wave vector of the phonons, $\omega(\mathbf{k})$, is called phonon dispersion. In the simplest case, the phonon dispersion for a one-dimensional chain of atoms is given by [34]

$$\omega = \sqrt{4C/M} |\sin(ka/2)| \quad 2.2$$

where ω is the angular frequency of the phonon, C is the restoring force constant, M is the atomic mass, k is the wave vector of the phonon and a is the lattice constant. The phonon spectrum consists of 3 acoustic and 3(N-1) optical branches, with N being the number of atoms in a unit cell of a three dimensional crystal. Furthermore, these phonon branches are split into two transverse and one longitudinal modes. The phonon dispersion is of primary importance to understand and interpret Raman spectra and it will be discussed in the following chapters.

2.2.2 Phonon Dispersion in Graphene

Since the unit cell of single-layer graphene (SLG) contains two atoms, A and B, there are six possible phonon dispersion branches as shown in the phonon spectrum of graphene in Figure 2.4. Three of these branches are acoustic (A) branches which exhibit no frequency at the Γ point, and the other three are optical (O) phonon branches. For one acoustic and one optical phonon band, the atomic vibrations are perpendicular to the sp^2 -plane of SLG and they

correspond to out-of-plane phonon modes. For two acoustic and two optical phonon bands, the vibrations are in-plane. These phonon branches are furthermore classified as longitudinal (L) or transverse (T) according to their parallel or perpendicular vibrations, with respect to the direction of propagating wave vector \mathbf{k} , respectively [35,36,37]. Hence, the six phonon dispersion curves along the high symmetry directions are named as; out-of-plane transverse acoustic mode (ZA), in-plane transverse acoustic mode (TA), in-plane longitudinal acoustic mode (LA), out-of-plane transverse optical mode (ZO), in-plane transverse optical mode (TO) and in-plane longitudinal optical (LO) phonon branches. These phonon branches are summarized in Figure 2.3 [36,38].

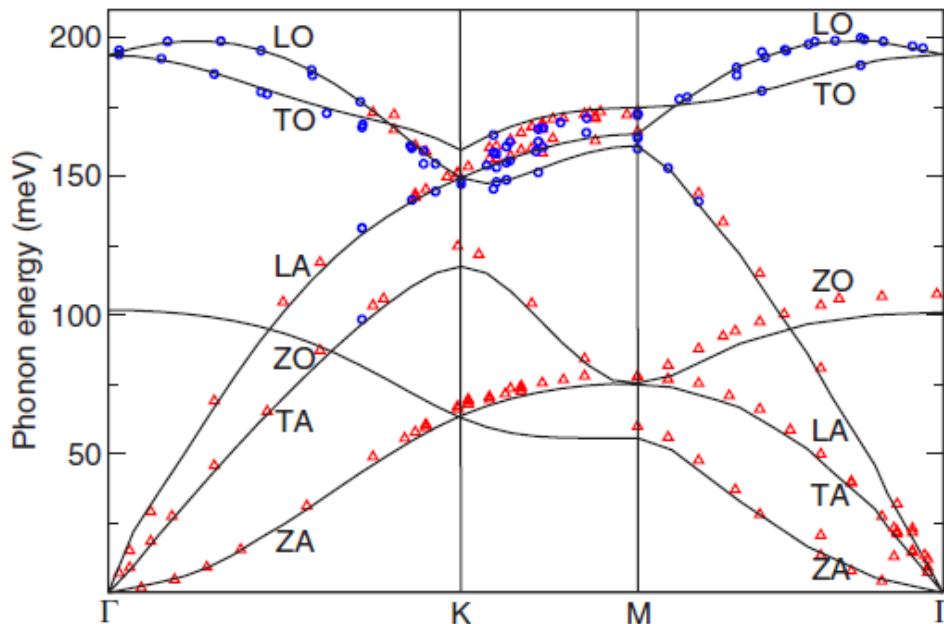


Figure 2.3. Calculated phonon dispersion of monolayer graphene showing the six phonon branches (adapted from References [36,38]).

The iTO and LO phonon branches are degenerate at the Γ point and according to group theory belong to the two dimensional E_{2g} representation. Consequently, these two branches are Raman active. At the K point the iTO phonon branch has A_{1g} representation, which corresponds to a breathing-like motion of the hexagonal rings illustrated in Fig 2.6 (e) [36,39]. Moreover, the derivation of iLO phonon branch at Γ point and iTO phonon branch at K point are discontinuous [36,37]. This phenomena is known as Kohn anomaly and it leads to a phonon softening of the phonons at Γ and K points [40].

2.2.3. Theory of Raman Scattering

When light interacts with matter, part of the photons are transmitted, while the rest interacts with the sample causing reflection, absorption, light scattering and luminescence. The nature of the interaction principally depends on the electronic and vibrational properties of the material. Raman scattering or the Raman effect is a process in which light is scattered inelastically by phonons and it is a powerful tool to probe the electronic and vibrational properties of solids and gases. The Raman effect was first observed by C. V. Raman in 1928 [41] and this discovery earned him a Nobel Prize in Physics 1930 "for his work on the scattering of light and the discovery named after him" [42]. Raman spectroscopy is considered to be a very versatile tool to study the carbon systems such as graphene and carbon nanotubes [43].

The light scattering process can be described by the interaction between photons, electrons, and the quantized atomic vibrations, i.e. phonons [44]. If the incident photon has the same energy level and wavelength as the emitted photon, this process is called Rayleigh scattering. Rayleigh scattering is an elastic event and does not involve any phonons. In contrast, Raman scattering occurs when the photons of the incident light interact with the phonons and go through energy exchange. As a result, the energy of the scattered photon can increase or decrease. This increase or decrease in energy level is known as anti-Stokes or Stokes Raman scattering, respectively. Compared to Rayleigh scattering, Raman scattering is a less common event, since only one in $\sim 10^6$ scattered photons contributes to the Raman signal [45]. However it can be steadily observed if a laser is used as an excitation source.

The types of scattering are illustrated in Figure 2.4. Here the incident photons excite electrons from the ground state E_0 to energetically higher states. The excited states can be either real or virtual depending on the energy of the incident photon. The excited electron can either create or annihilate a phonon, resulting in a decrease or increase of the electron's energy, respectively. Thus the emitted photon has either a smaller or a higher energy than the incoming, initial photon. Consequently, a Stokes process corresponds to phonon creation whereas in an anti-Stokes process a phonon is absorbed. The energy or frequency difference between the photons during the scattering process is called Raman shift and is typically measured in units of reciprocal centimeters (cm^{-1}). At low temperatures no excited phonons exist in the material, therefore the majority of Raman scattering is Stokes scattering. Due to

this fact Stokes scattering is exclusively used in conventional Raman spectroscopy [46]. The Raman spectrum for a material is actually a record of the frequency shift between incident and scattered light, and is a fingerprint of the material.

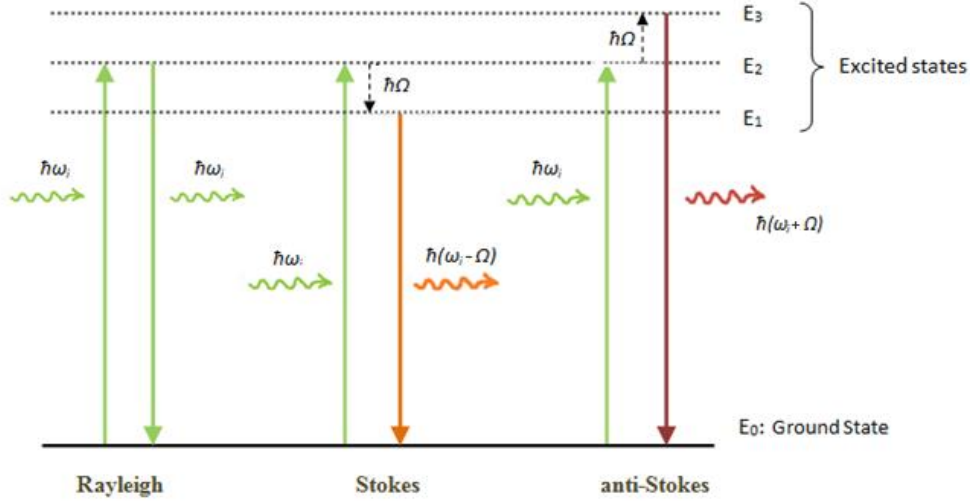


Figure 2.4: Three forms of scattering. $\hbar\omega_i$ and $\hbar\Omega$ are the energies of the incident photon and the phonon, respectively.

In a Raman process the energy conservation is given as:

$$\hbar\omega_i = \hbar\omega_s \pm E_{phonon}$$

where \hbar is the Planck's constant divided by 2π , ω_i and ω_s are the frequencies of incident and scattered photons, respectively. In the process momentum must be conserved as well. Thus, the difference between the wavevectors of the incoming and outgoing photons must be equal to the wave vector of the phonon or ,

$$\mathbf{k}_i = \mathbf{k}_s \pm \mathbf{k}_{phonon}$$

Here \mathbf{k}_i , \mathbf{k}_s and \mathbf{k}_{phonon} are the wave vectors of incident photon, scattered photon and phonon respectively. + and - signs in the energy and momentum conservation correspond to Stokes and anti-Stokes processes, respectively.

In the first order Raman scattering, since the momentum of light in the visible range is rather small compared to the size of the Brillouin zone, scattering mainly occurs near the Brillouin zone center (Γ point). Therefore, the phonons participating in this process are Γ -point phonons with $\mathbf{q} \approx 0$.

In the second order Raman scattering the conservation rule may be written as

$$\mathbf{q}_1 + \mathbf{q}_2 \approx 0$$

which implies that two-phonon scattering process is not limited to particular points in the Brillouin zone, and the contribution from points throughout the Brillouin zone is also possible. In this case, momentum conservation can be satisfied by two phonons with opposite wave vectors or by defect scattering as well.

In classical theory, polarizability plays an important role in activation process of Raman scattering, such that the only Raman active atomic vibrations are those which cause a change in the polarizability of the electron clouds in an atom. This relation can be written as

$$\frac{\partial \alpha}{\partial Q} \neq 0$$

meaning that the change in polarizability ($\partial \alpha$) with respect to the change in vibrational amplitude (∂Q) must be non-zero. This is the basis for Raman selection rules from the classical point of view.

2.2.4. Raman Spectroscopy of Single-Layer Graphene

Raman spectroscopy is one of the most informative spectroscopic methods up to date and is a key tool for identification and characterization in graphene research [47]. It is a powerful, non-destructive technique for identifying the number of layers, structure, doping and defects in graphene [48,47,49]. In graphene lattice, the in-plane stretching of C-C atoms create strain induced polarizability and causes disruption of hexagonal symmetry, which in turn makes the graphene surface Raman active [50]. The Raman spectrum of mechanically exfoliated pristine and defected monolayer graphene are shown in the Figure 2.5. In this spectrum the major features are the *G* band at around 1580 cm⁻¹ and the *2D* band at around 2700 cm⁻¹ obtained by using green laser excitation at 2.33 eV. Another important peak appears at about half of the frequency of the *2D* band (~1350 cm⁻¹) which is known as *D* band. This peak has generally a lower intensity than *G* and *2D* peaks and is observed in defected graphene samples and at the edges of the graphene flake. Additionally to the *D* peak there is another weak defect-induced *D'* band which is observed at around 1620 cm⁻¹. There is also a low intensity peak at ~2450 cm⁻¹, which we call *iTOLA* (also called *G**).

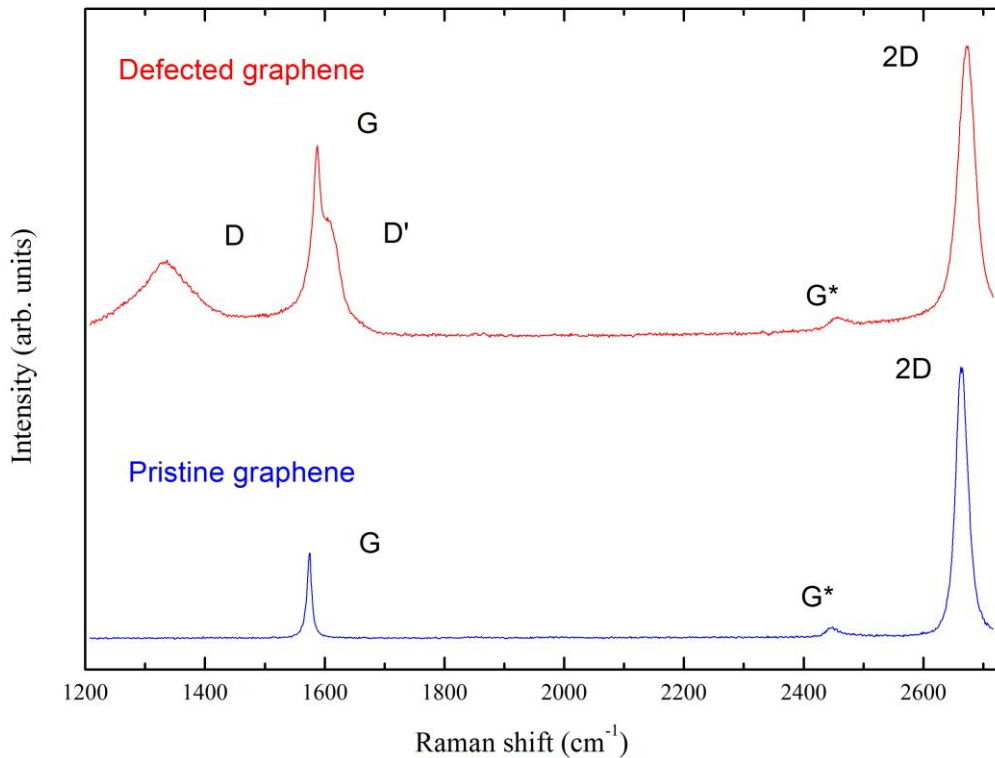


Figure 2.5. Raman spectrum of pristine and defect-free monolayer graphene under green laser illumination (532.3 nm, 2.33 eV).

***G* band in SLG**

We will recall the phonon dispersion of monolayer graphene in order to understand the origins of the Raman active modes (see Fig. 2.3). The *G* peak is due to the bond stretching of all pairs of A and B atoms and hence depends mainly on the amount of carbon atoms in the laser spot [47]. Due to this fact, the *G* peak intensity will increase with increasing thickness of graphene [51]. This peak is a first order Raman process and originates from the doubly degenerate *iTO* and *iLO* phonon branches at the Γ point (E_{2g} symmetry) [37]. The name *G* comes from graphite since this band is a characteristic peak in all graphitic materials [52]. Fig. 2.6 (a) illustrates the process giving rise to the *G* band [37]. This band does not exhibit dispersive behavior in its position but is remarkably sensitive to charge transfer, and therefore is an important indicator of doping [37]. *G* mode is also sensitive to strain effects and can be used to probe the surface modification in sp^2 system. In a typical Raman spectra of pristine SLG, *G* peak has a full width at half maximum (FWHM) of $\sim 16 \text{ cm}^{-1}$ [53].

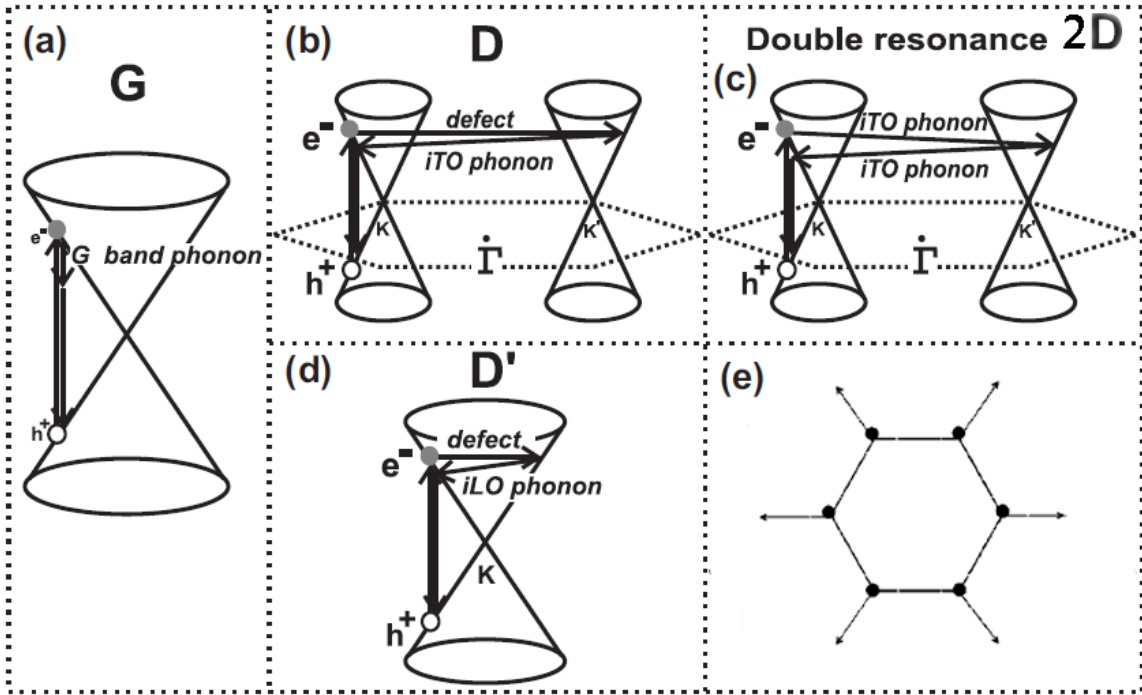


Figure 2.6. (a) First-order Raman process giving rise to the G peak. (b) double resonance scattering process involving one iTO phonon and defect scattering in D mode , (c) $2D$ mode and (d) D' mode ([image adapted from Ref. [37]). (e) Breathing motion of a sixfold ring in SLG showing A_{1G} symmetry. Adapted from ref. [39].

2D band in SLG

The $2D$ band, which is also called G' in literature, originates from a second order Raman process involving a double resonance (DR) scattering event between K and K' points [54]. This process is illustrated in Fig. 2.6 (c) [37]. Here, the electron is first excited resonantly by an incoming photon to an excited state around the K point. The electron is then scattered inelastically by a phonon with momentum q to another excited state belonging to a circle around K' point. This neighboring energy state at K' is also an eigenstate of the system. In the total process, momentum and energy must be conserved, hence a second phonon with opposite momentum of $-q$ is required to backscatter the electron to initial k -space position near the K point. Consequently, the electron emits a photon by recombining with the corresponding hole in its initial state. Since two iTO phonons contribute to the $2D$ mode, its frequency is roughly twice the frequency of the D mode. These iTO phonons are non-degenerate phonon branches associated with A_{1G} vibrational mode at K or K' point [37]. The

motion of the carbon atoms related to the $2D$ peak is shown in Fig. 2.6.(e), which is called breathing like motion. It can be seen in Fig.2.5 that the $2D$ mode is a single, sharp peak having a higher intensity than the other bands which is characteristic to single-layer graphene (roughly 4 times of G peak intensity in pristine graphene). This peak is a very helpful feature of SLG to identify and distinguish the monolayer graphene from multi-layer graphene samples. The well-known features of this peak are its strong dispersive behavior due to the DR process and its sensitivity to defects. As the defects increase the intensity of the $2D$ peak decreases.

D band in SLG

The defect induced D band also originate from the DR process and is a breathing mode of A_{1G} symmetry at the K point (see Fig. 2.6 (e)). However in this case the two scattering events consist of one elastic and one inelastic scattering events. The elastic scattering event occurs due to the scattering from a defect and the inelastic backscattering event results from emitting or absorbing a phonon. Fig. 2.6.(b) depicts the process giving rise to D band [37]. This band is not observed in pristine graphene or in graphene with perfect crystal quality (see Fig. 2.5). It only appears at the presence of structural disorder and also at the edges of graphene. The D peaks exhibits a dispersive behavior [55] and its intensity depends on the amount of disorder and crystallite size. The DR process for D and $2D$ bands are called *inter-valley* process because it connects two inequivalent K and K' points in BZ [56].

D' band in SLG

The D' band, which is induced by defects, also involves the DR process and is associated with LO phonon . However in this case the process occurs at around one K point [37]. In the process, the electron is scattered to neighboring excited state on the same circle around K or K' point and an iLO phonon is involved, as shown in Fig. 2.6 (d) [37]. The D' peak shows a weak dispersive behaviour because of the slope of the iLO phonon near the Γ point (see Fig. 2.3) [37]. Since this process occurs around the same point, it is called *intra-valley* DR process.

2.2.5. Defect Characterization by using Raman Spectroscopy

Understanding the influence of defects on graphene is an important aspect to gain an insight in its fundamental properties. In general defects are defined as anything that breaks the symmetry of the honeycomb lattice [57]. There are several type of defects in graphene such as edges, vacancies, grain boundaries, ad-atoms and sp^3 -type defects. As we mentioned in previous section, presence of defects induces D and D' modes in Raman spectra of SLG . These modes are also observed in Raman spectra of graphite. The earlier studies conducted on graphite has given an insight into the origin of defect induced bands and characterization of defects [58]. The crystal grain size and the amount of defects in graphitic materials can be estimated by analyzing the intensity of the D mode [58]. Based on this study, it was proposed that the intensity ratio of the D and G modes (I_D/I_G) is inversely proportional to the crystallite size (L_a), which is known as Tunistra and Koenig (TK) relation [58]

$$I_D/I_G \sim 1/L_a$$

However this approximation was not completely accurate. As the grain size becomes too small ($L_a \approx 3$ nm), the ratio (I_D/I_G) reaches its maximum and decreases toward zero for $L_a < 3$ nm because of the decrease in amount of sp^2 hexagonal rings. In this case TK relation is not valid anymore and the ratio follows as [59]:

$$I_D/I_G \sim L_a^2$$

The complete relation is shown in Fig. 2.7 [59]. The evolution of I_D/I_G was further explained by Ferrari and Robertson by introducing three-stage model of increasing disorder which they call "amorphization trajectory" [60]. This model was first introduced for disordered and amorphous carbon and later reviewed for graphene based materials [47]. The three stages are:

- (1) *graphite* \rightarrow *nanocrystalline graphite (nc-G)*
- (2) *nanocrystalline graphite* \rightarrow *amorphous carbon (a-C)* and
- (3) *a-C* \rightarrow *high sp^3 amorphous carbon*

which are schematically shown in Fig. 2.8. [60]. In the study of graphene, the first two stages are most relevant due to its two dimensional nature, therefore only these two regimes are summarized here. In the first stage, graphite is transformed to nanocrystalline carbon where the TK relation is obeyed. The D and D' peaks appear and I_D/I_G ratio increases with increasing disorder. All peaks broaden and the average G peak position moves to higher

values (ca. $\sim 1600 \text{ cm}^{-1}$) as shown in Fig. 2.9 [57, 60]. In the second stage, the TK relation fails and I_D/I_G starts to decrease with increasing disorder as in Fig. 2.9. This decrease in I_D/I_G is due to the distortion and reduction of sp^2 carbon rings. The G peak position decreases to lower values ($\sim 1510 \text{ cm}^{-1}$) and its intensity exhibits a dispersive behavior.

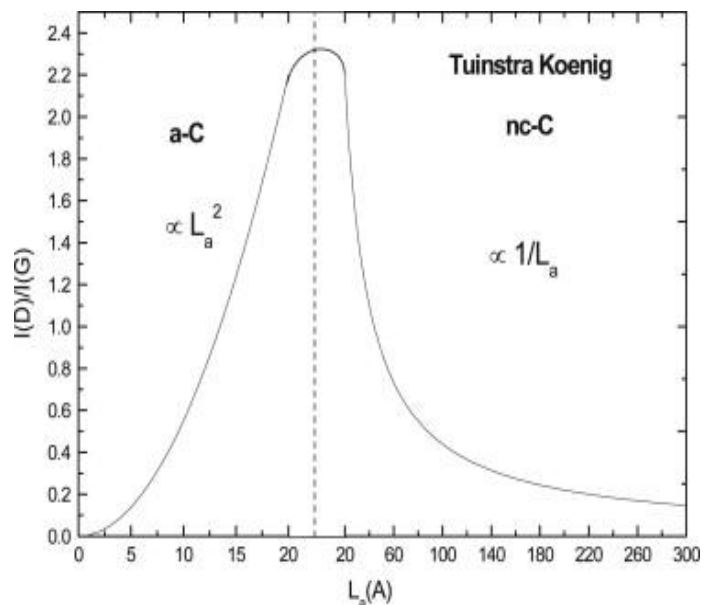


Figure 2.7. The intensity ratio of D and G modes as a function of disorder (measured at 514.5 nm excitation). Taken from Ref. [47].

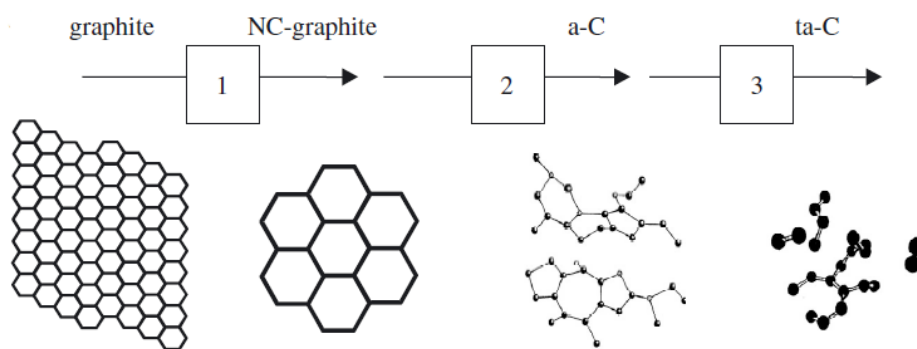


Figure 2.8. Amorphization trajectory for carbon based materials. Taken from Ref. [60].

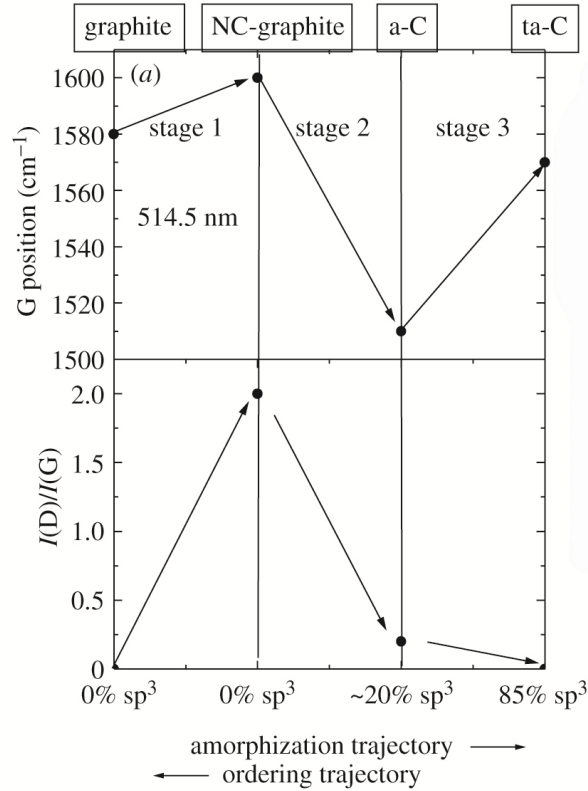


Figure 2.9. Evolution of G peak position and I_D/I_G with increasing disorder. Taken from Ref. [60]

2.2.6. Doping in Graphene

Doping plays a key role to control the semiconducting properties of materials in semiconductor physics. Even though graphene has no band gap, doping is regarded as one of the most feasible methods to modify its electronic properties and obtain a semiconducting gap [61]. As mentioned before, Raman spectroscopy is a powerful tool also for monitoring the charge impurities and doping in graphene [49]. There are two main characteristics in Raman spectra of graphene to monitor the doping; the position shift of the G and $2D$ peaks. Fig. 2.10 (a) shows the Raman spectra of SLG at different values of top-gate voltage. Fig. 2.10 (b) and (c) plots the evolution of Raman parameter (G and $2D$ peak positions, and FWHM of the G peak) as a function of doping [49]. The G mode position increases with an increasing amount of doping, hence is a key tool to determine the amount of excess charges in graphene. The shift of the $2D$ mode responds differently to electron and hole doping such that it undergoes an upshift for hole doping and down shift for electron doping [49]. The ratio of the intensities of the G and $2D$ bands (I_{2D}/I_G) is also sensitive to doping in graphene however the change in

2D intensity may occur due to increase in defects as well, hence causing an ambiguity. Additionally, the G band stiffens and sharpens for both electron and hole doping [49]. Furthermore, when analyzing the doping in graphene, one has to take into account the other parameters such as disorder, temperature and strain that have an influence on Raman bands as well. Due to this fact it becomes a challenge to analyze and interpret the Raman data of defected and doped graphene.

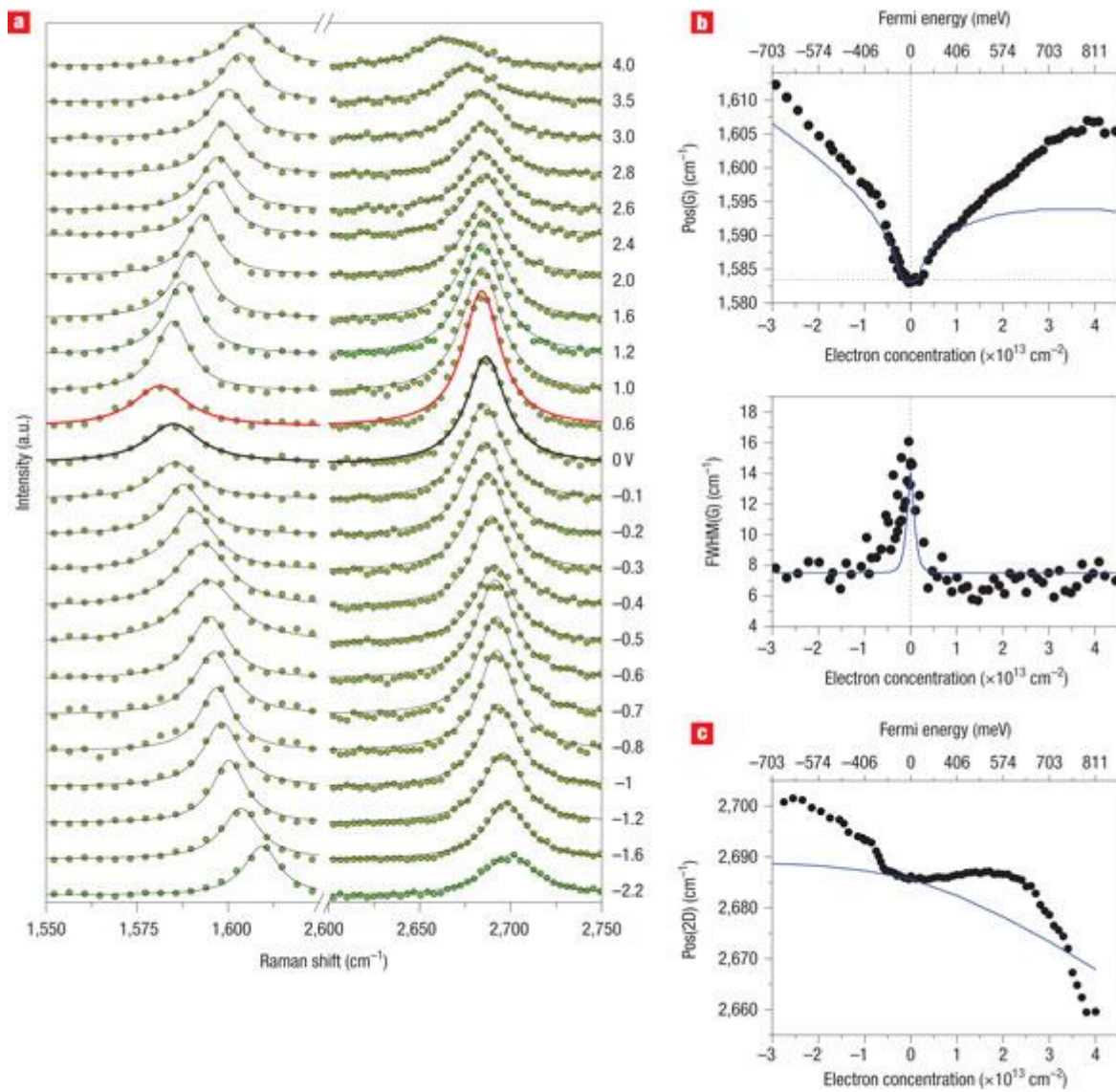


Fig. 2.10. a) Raman spectra of SLG as a function of gate voltage at values between -2.2 V and +4.0 V. The red line corresponds to the Dirac point b) G peak position and FWHM as a function of hole and electron doping. c) 2D peak position as a function of electron and hole doping. (Taken from Ref. [49])

Chapter 3

Experimental Methods

3.1. Samples

Graphene samples were prepared by using mechanical exfoliation method. Natural graphite flakes are distributed on a stripe of scotch tape and subsequently folded and peeled apart. This process is repeated several times in order to obtain thin enough flakes. The cleaved graphite is then transferred onto a Si/SiO₂ substrate by placing the tape onto a substrate and pressing it gently where it randomly deposits graphene and graphite of a variety of number of layers.

Monolayer graphene flakes are first identified under an optical microscope by their faint contrast. Consequently the single-layered flakes were identified via the shape of the Raman 2D band using the micro Raman spectroscopy [62]. One of the samples is shown in Fig. 3.1. The optical images of the samples were obtained by using Olympus BX51M microscope with 100x objective.

The substrates used are slightly p-doped silicon (Si) with a (100)-oriented surface and with a SiO₂ thickness of 100 nm. These substrates were also equipped with geometrical markers for unambiguous identification of samples' positions.

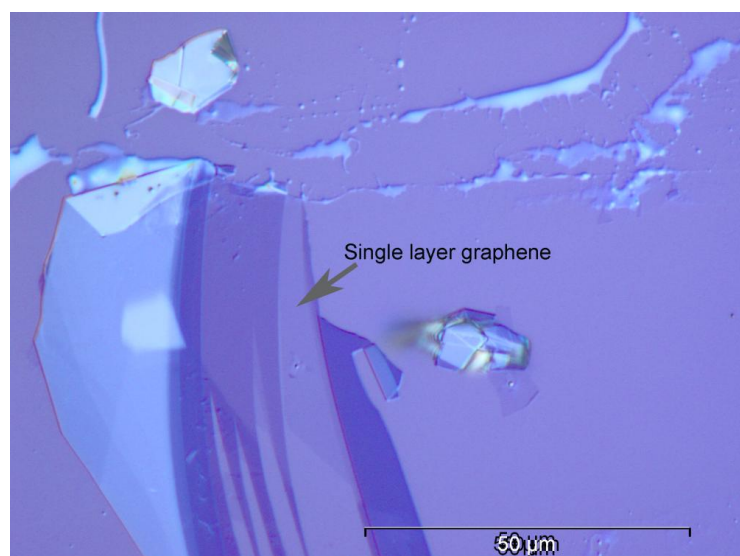


Fig. 3.1. Mechanically exfoliated single-layer-graphene.

Two different laser sources were used to irradiate the samples: by using a frequency-doubled Nd:YAG laser with 532 nm wavelength and tunable Ti:Sa pulsed laser system with 370 nm wavelength.

One of the flakes was transferred on a transmission electron microscopy (TEM) grid to obtain freestanding monolayer graphene by using the first method explained in Ref. [63].

Additionally, one of the samples was heated for 5 minutes at 200 °C in air on a heating plate.

3.2. Raman spectrometer

The Raman spectra were acquired in confocal micro Raman setup in the backscattering configuration under ambient conditions. The spectra of samples were measured using a LabRAM HR800 Raman Spectrometer by Horiba Jobin Yvons using a Nd:YAG laser source with excitation wavelength of 532.315 nm i.e., an excitation energy of 2.33 eV. The laser was focused with a 100x objective with a numerical aperture of NA=0.95. The laser spot size was estimated by using the Raman line scan across a thick graphite flake and recording the signal from the silicon substrate. This data was fitted by cumulative distribution function. Afterwards, the laser spot size was extracted to be approximately 740 nm from the fit parameters. Fig. 3.2 shows the intensity of the silicon signal versus position graph.

600 lines/mm and 1800 lines/mm gratings were used to record the spectra. The laser power was set to a maximum value which varies between 33mW and 40mW. The Raman spectra were calibrated by using standard atomic emission lines of Neon. The laser power was measured under the objective with a laser power meter. The spectra were fitted by using *peak-o-mat* and *Origin 8* software.

In the time-resolved Raman mapping the samples were irradiated with Nd:YAG laser and at the same time the Raman data was recorded every second. The duration of the laser irradiation varied from 5 minutes up to 30 minutes.

To perform mappings on selected areas a Märzhäuser xyz-scanning stage was used in combination with LabRAM HR800 spectrometer shown in Fig. 3.3. The step widths of ≈ 250 nm, ≈ 400 nm, and ≈ 500 nm were used during the spectral mapping measurements on

selected areas. The Raman data were mainly fitted by using a python script with NumPy and SciPy extensions. The script can be seen in Appendix A.

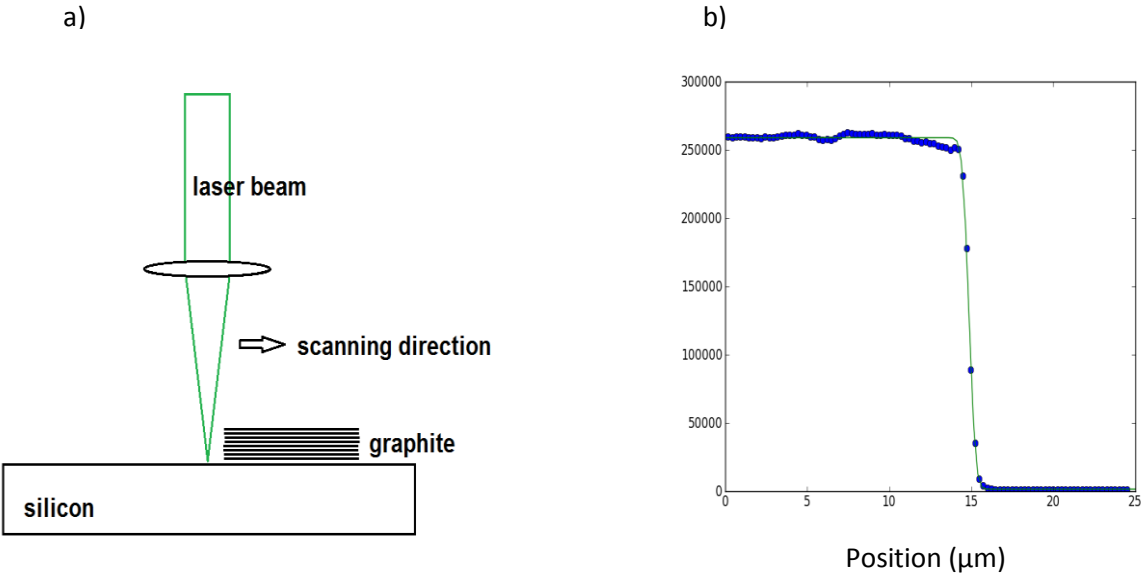


Fig. 3.2.(a) Schematic illustration of the line scanning of silicon (b) Silicon signal obtained from the line scan versus position graph. The y axis shows the intensity of the silicon signal and the x axis is the position in μm . The fit formula follows as $0.5 \cdot I \cdot (1 - \text{erf}((x - \mu) / (\sqrt{2} \cdot \sigma)))$

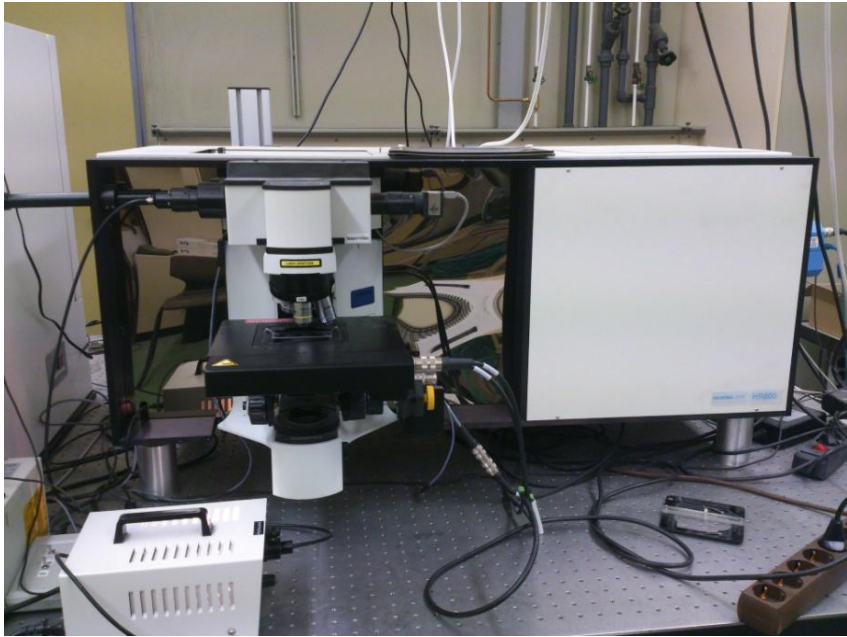


Fig. 3.3. The LabRAM HR800 Raman spectrometer used for the experiments.

3.3 Pulsed Laser

A tunable Ti:Sa laser system with second harmonic generation (SHG) pumped by a frequency doubled 10 kHz-pulsed Nd:YAG laser was applied as a second source to irradiate the samples. The wavelength of the laser with 30 ns pulse width was set to about 370 nm. The exposure time was controlled manually and is about less than a second. One of the flakes was then studied by AFM.

3.4 AFM measurement

Atomic Force Microscopy (AFM) is a very sensitive and effective method to investigate the topography of a sample and obtain high-resolution images of its surface. The main advantage of AFM to other Scanning Probe Microscopy (SPM) techniques is that the surface of the measured sample does not necessarily have to be conductive and hence all kinds of specimen can be investigated. The setup consists of a cantilever with a very sharp tip made of silicon nitride (SiN), laser focused on this tip, a piezo stage to move the sample and a photodiode array for the detection of reflected laser beam. AFM uses inter-atomic forces between the tip and a surface for the measurement of the surfaces. The cantilever holds a sharp tip which comes into contact with the sample's surface. During the surface scan, the height of the cantilever changes according to the topographic layout of the surface. The height profile of the sample is calculated from the position of the reflected beam on the photodiode. The AFM images presented in this thesis were acquired in a non-contact mode by using a Park Systems XE 100 AFM shown in Fig. 3.4.



Fig. 3.4. XE 100 AFM from Park Systems
The images were processed with WSxM 5.0 Developer 6.3 software. A sample AFM image of exfoliated single layer graphene is shown in the Fig. 3.5 (a) and (b).

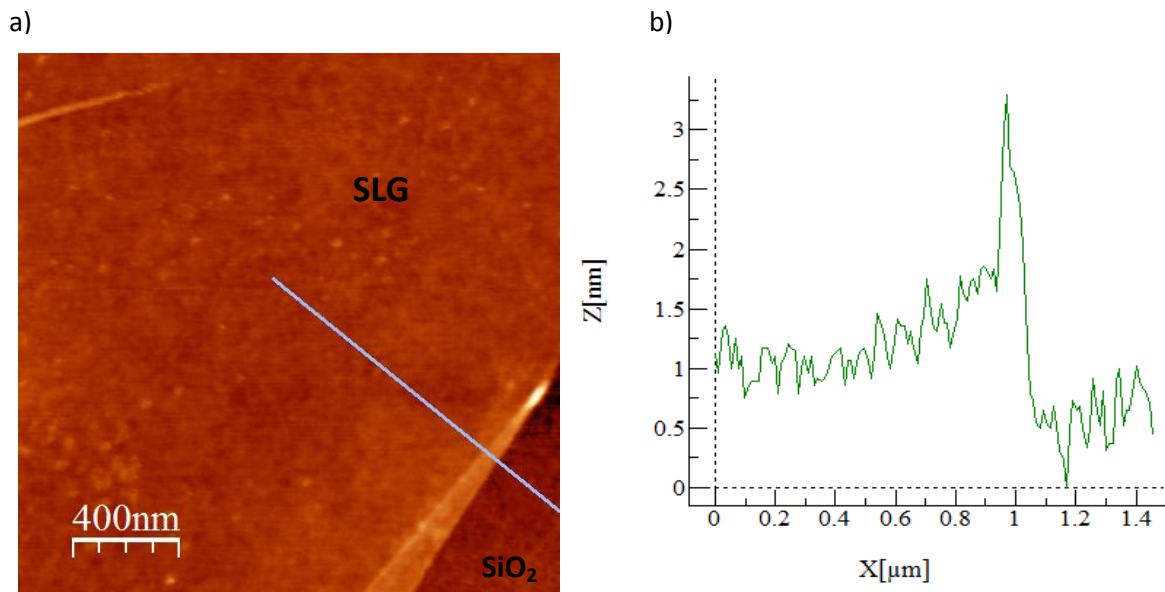


Fig. 3.5 (a) AFM image of exfoliated SLG. (b) Height profile analysis across the line shown in (a).

Chapter 4

Results and Discussion

In this chapter we present the analysis and interpretation of Raman measurements and corresponding AFM images, and compare some of our results with the results from the literature. Our research platform is based on laser treatment of single-layer graphene followed by defect analysis as well as understanding the mechanism behind the possible structural modifications. The measurements of the two samples with interesting results are presented in the following sections. In the first section the experimental results from Raman measurements will be discussed. In the second section pulsed-laser induced changes are to be discussed.

4.1. Laser Exposure and Raman Spectrum

4.1.1. Overview of the Raman Spectrum

After exfoliation and identification of SLG, the sample was exposed to a Nd:YAG laser under ambient conditions. The process was repeated many times on different SLG flakes. We will present here one representative flake with different laser treated regions. All the flakes show more or less the same behaviour and the results could be reproduced on other flakes very easily. Fig. 4.1 (a) and (b) shows an optical and AFM images of the single-layer graphene sample before and after the laser exposure, respectively. There are no visible changes in the optical images before and after the laser radiation, however the changes are clearly observed in the AFM images.

The maximal laser power was applied during the irradiation and the idea behind that was to see the behavior of graphene under this specific condition. Fig. 4.2 shows the time evolution of Raman spectra of graphene under irradiation with a laser of 532 nm wavelength with 33 mW power. The spectral changes are more obvious in the expanded graphs in Fig. 4.3 (a) and (b), which depict the evolution of the D, G, and 2D, iTOLA modes in a magnified scale, respectively. As it can be seen from the images the spectra undergoes a dramatic change, especially in the D and G modes range between 1250cm^{-1} and 1700cm^{-1} . As discussed in the

second chapter, the appearance of D and D' modes are indication of structural defects in graphene crystal.

Here the changes on the Raman spectra of laser-radiated SLG flake are briefly described. These spectrum belong to the first modified area shown in Fig. 4.1.(b). A shape analysis of the 2D band has been successfully used to identify the single-layer graphene [62].

In the first spectra which is indicated with black color in Fig. 4.2, the 2D peak at around 2654 cm^{-1} clearly indicates that the flake is a monolayer. The D peak is not observable in our pristine flake which shows that we have a SLG with good crystal quality and undetectable small amount of defects. The G peak appears at around 1575 cm^{-1} .

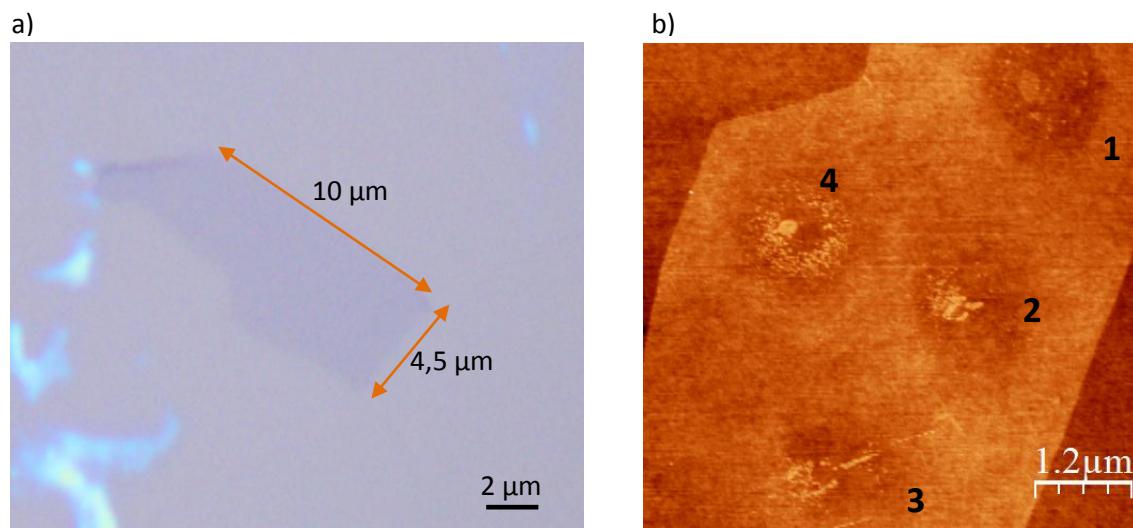


Fig. 4.1. Optical and AFM images of a single-layer graphene a) before and b) after the laser exposure. The numbers on the AFM image indicate the laser-induced modifications on the graphene flake. The optical image was rescaled manually and the size of the flake is obtained from AFM image.

In the second spectra (red line) of Fig.4.2, there is a strong increase in the background and the D peak appears at around 1340 cm^{-1} . The intensity of the G peak also increases. 2D mode intensity also increases slightly. It is important to note here that, for the intensity of the G mode, we use the integrated area under the G peak. In general, the area under the peak is used as an intensity for small amount of disorder or perturbations, since the area under each peak represents the probability of the whole process in consideration with uncertainty [57, 64]. In our case we consider to have small amount of disorder since we are using a laser source and not an ion or electron bombardment.

In the third spectrum (green color) we see a very large and broad D mode or combination of more than one peak. The D' mode next to the G mode is also clearly observed. The area under

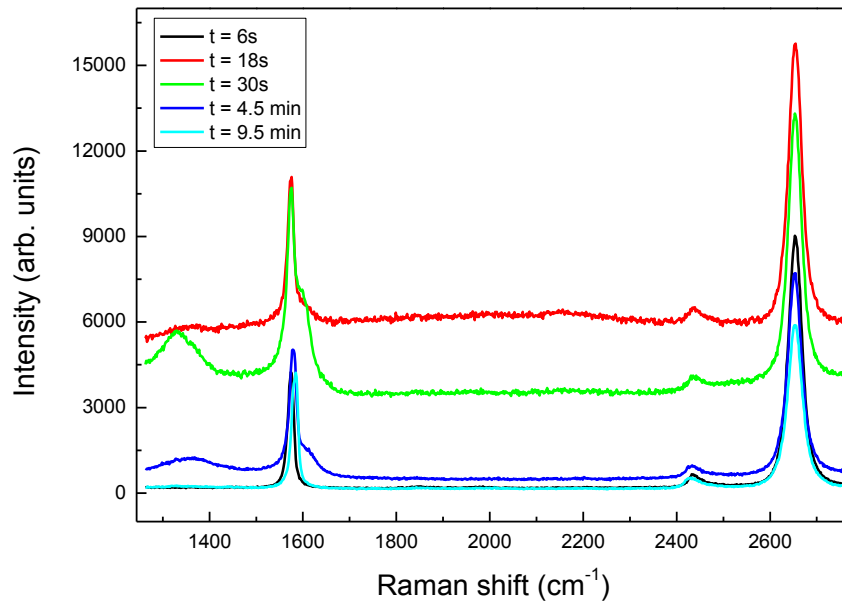


Fig. 4.2. Laser-induced change in the Raman spectrum of SLG radiated with 532 nm laser with 33mW power. Each spectra corresponds to a different time interval.

the G mode continues to increase whereas the background is decreasing. There is again a slight increase in the 2D mode intensity. We also observe that the background spectrum between 1200 and 1600 cm⁻¹ increased noticeably.

In the fourth spectrum (blue color) which corresponds to the 4th minute of the irradiation, we observe a decrease in the D mode and background. The G mode intensity also decreases and besides it shifts to the higher frequency (also known as a blue shift). 2D mode intensity drops significantly.

In the final spectra (cyan color) the graph resembles very much the initial spectrum of pristine graphene however with some changes. The D and D' modes are almost disappeared and only very small D mode can be observed in a magnified graph. G mode also looks similar to the initial spectrum, however it has shifted its position from 1574 cm⁻¹ to 1582 cm⁻¹. 2D mode has decreased in intensity compared to the initial spectrum.

There are a few possible explanations for these changes in the Raman spectra of SLG. Firstly, it is known that laser irradiation causes heating of the electronic system [65]. Therefore, we

believe that effects of the laser-induced heating play a key role in the process. In general during the Raman measurements, a laser with less than 1 mW power is used in order to avoid laser-induced heating. Since we use here much higher laser power, obviously the influence of heating must be taken into account.

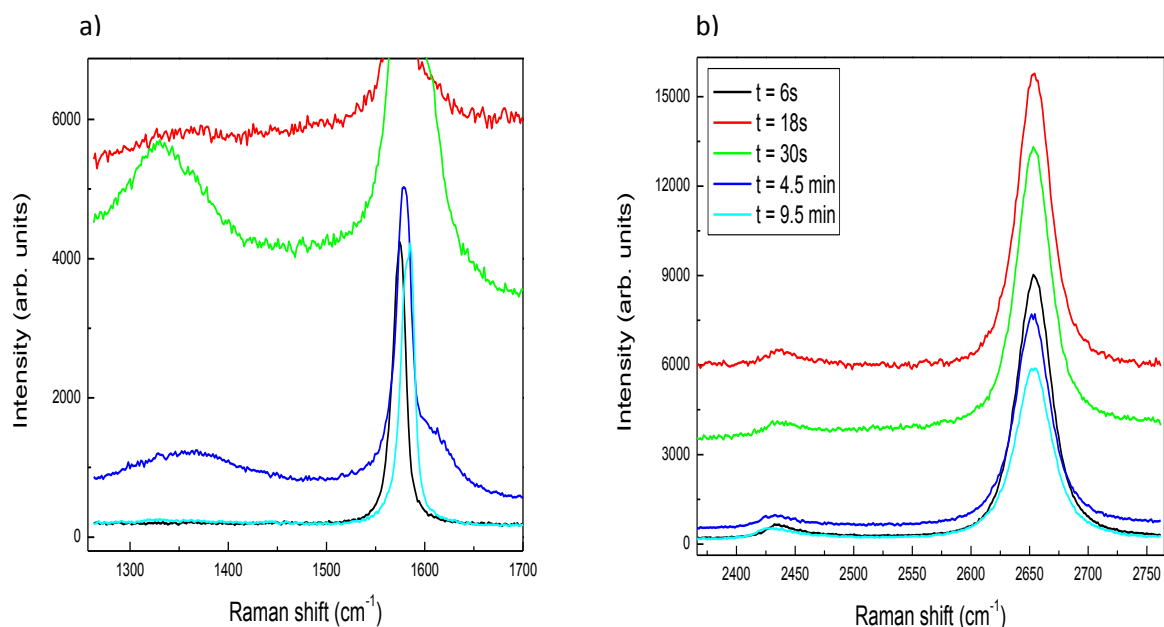


Fig. 4.3. Magnified image of (a) D and G modes and (b) 2D and iTOLA modes of the previous graph. The strong "jumps" in the G and 2D modes are due to the increased background.

Secondly, the experiments were conducted under ambient conditions and as a result photo-induced chemical reactions with surrounding molecules are believed to be among the dominant processes. These molecules are assumed to be mainly oxygen (O_2) and water (H_2O) molecules from the atmosphere. Especially oxidation of SLG is believed to occur during the laser radiation. It is also well-known that the residual water molecules exist also between the graphene surface and SiO_2 substrate.

Thirdly, it was previously reported that, laser irradiation can induce structural modifications in SLG crystal. An SLG crystal undergoes a local structural change from a single crystalline structure to an interconnected nanocrystalline structure under the laser spot [17]. Considering also the three-stage increasing disorder model introduced in section two, we believe that this process might be responsible for the G mode upshift.

Another interesting idea that was introduced recently is that, adhesive polymers left on the graphene flake during the mechanical exfoliation process are assumed to be the origin of the new D and G peaks in the Raman spectra of annealed graphene [66, 67]. Here, the tape residues are assumed to be a source for amorphous carbon (aC) during the annealing process. Since we observe similar peaks around the D and G modes, we believe that this process might be responsible for the drastic changes in our spectra.

Experimental studies on mechanically exfoliated graphene on various substrates have shown that weak interaction between graphene layer and various substrates have negligible effect on Raman spectra [68]. However, we cannot neglect the effect of the substrate in this specific case since we deal with a heated graphene layer which subsequently affects the substrate underneath. This can also result in etching of graphene via reduction of the SiO₂ which will be discussed later [69].

Besides that, the doping is also an important factor affecting the Raman spectra, as mentioned in section two. Here, the water and oxygen are believed to be among the dominant doping species. We might observe several stages of doping level in our graphene flake. At the beginning, the dopants are assumed to be removed due to the laser heating, however, when the laser is turned off, the adsorption of additional molecules from ambient air is thought to take place.

In the next sections we will analyze the individual Raman peaks and Raman maps of the sample graphene flake in detail and explain how these changes support our assumptions. Similarly we will also point out the drawbacks of these assumptions. It is more probable that we have a combination of few processes occurring simultaneously or at different stages of the whole process.

4.1.2. Time resolved Raman measurements

In the previous section only five spectra at different time intervals were introduced. In this section the evolution of each peak over the whole process is discussed. The fitting script was written by using python program. (see Appendix A). For each data point on these curves a Raman spectrum was acquired in the range from 1200 to 2800 cm⁻¹ with a 1 second integration time. The results shown here are repeated several times and they are reproducible.

D mode

Fig. 4.4, 4.5 and 4.6 depict the evolution of intensity, position and full width at half maximum (FWHM) of the D mode with time, respectively. These graphs were fitted with a single

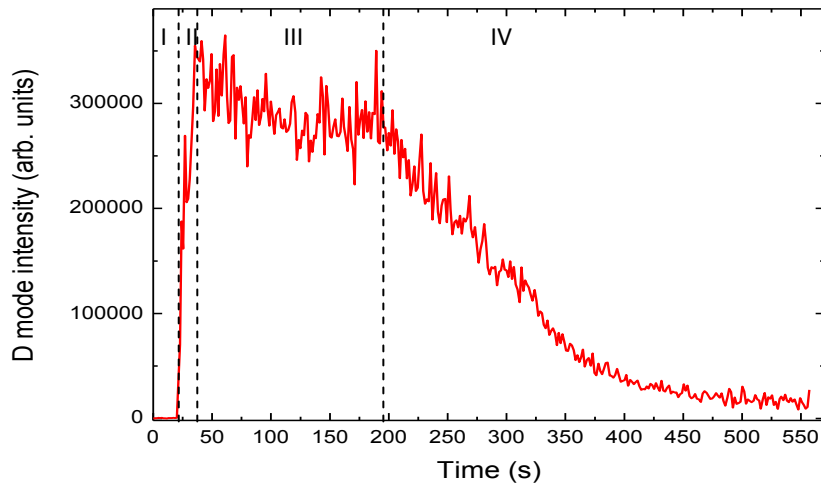


Fig. 4.4. Time evolution of D mode intensity.

Lorentzian function and belong to the second point area shown in Fig. 4.1(b).

The intensity evolution graph can be divided into four stages. The first stage is a threshold stage where no change is observed and the D mode intensity is zero. The time interval for this stage is around 20 seconds for the second laser-radiated area shown in Fig.4.1(b). This time ranges between 15 and 24 seconds for other modified areas. We have observed that the threshold stage time decreases with increasing laser power, i.e. the more power is applied the faster is the transition to the second stage. This can be explained by the rate of temperature increase. An increase in the laser power increases the heating rate of the irradiated region and hence affecting the heating-induced reaction rate.

The second stage is a stage where drastic changes start to occur. D mode intensity starts to increase dramatically as shown in Fig. 4.4. The intensity increase continues for 10-15 seconds and reaches its highest value. This means that the dominant defects are formed immediately at the beginning of the process. This stage is probably the most interesting part of the whole process because it plays a key role for understanding it.

In the third stage, there is a saturation of the D mode with slight decrease. The D mode intensity stays more or less constant in this period. The time interval lies between 35 s - 190 s.

In the final stage, the D mode intensity exhibits a steady decrease and eventually disappears. It does not go exactly to zero but has almost the same value compared to the initial spectra. This behavior seems very puzzling and it remains still as an unknown. After a 30 minutes of high power laser radiation, it seems like graphene survived without a damage. However, it

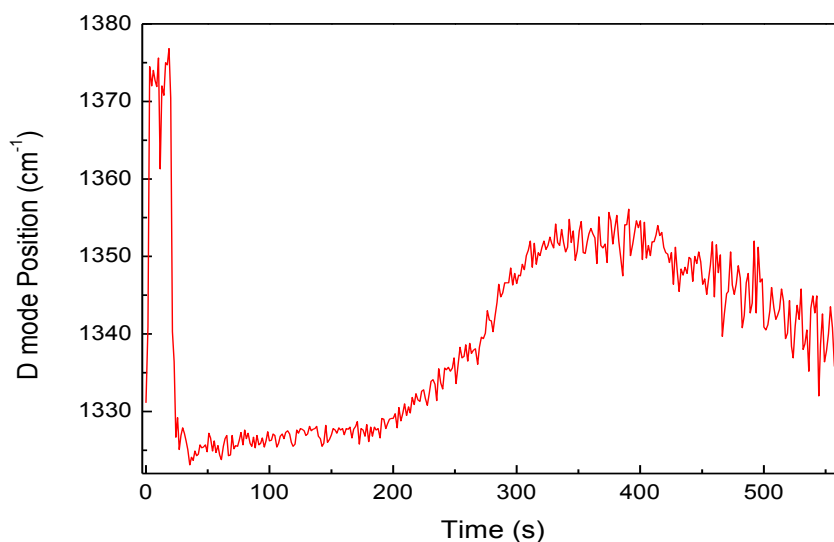


Fig. 4.5. Time evolution of the D mode position.

was reported previously that, even at lower laser powers, graphene undergoes a structural modifications, namely nanocrystallization [17]. Figure 4.5 shows the position versus time graph of the D mode. At the first 20 seconds there is a large noise in the spectrum since there is no significant D mode to fit. After this stage, the D mode appears nearly at 1325 cm^{-1} and with a slight upshift stays constant till around 190 seconds. After 190 seconds D mode undergoes a significant upshift till approximately 1355 cm^{-1} which corresponds to 4.3 minutes and then starts to downshift. The final value of the D mode position in the spectrum is 1340 cm^{-1} .

Fig. 4.6 shows the evolution of FWHM over the whole process. Here again we see a noisy data at the beginning of spectra (approx. first 21 seconds) because of absence of the D mode. At the next stage the D band has a FWHM value of approx. 106 cm^{-1} which is very broad for single layer graphene. After ~ 190 seconds, the spectra becomes even broader up to 135 cm^{-1} and after 4.3 minutes it becomes again very noisy. The changes in intensity, position and FWHM of the D mode follow almost the same time intervals with slight differences. The time dependent changes of the previous three graphs are shown together in Fig. 4.7. Here we can compare the time intervals where the changes take place.

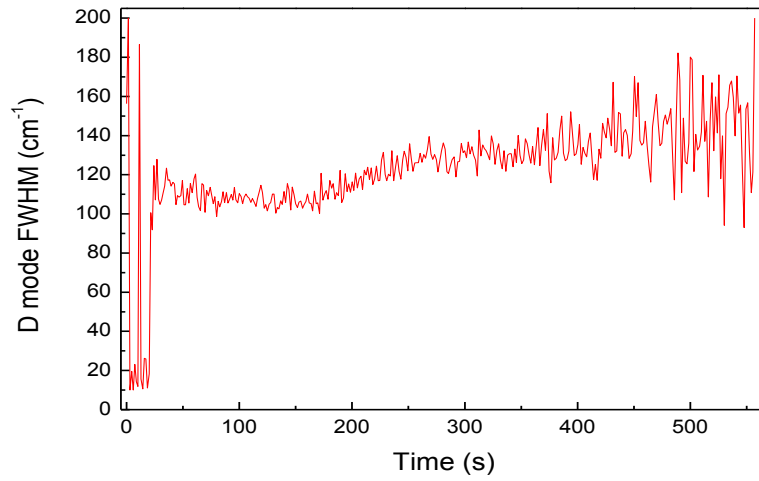


Fig. 4.6. Time evolution of the D mode position.

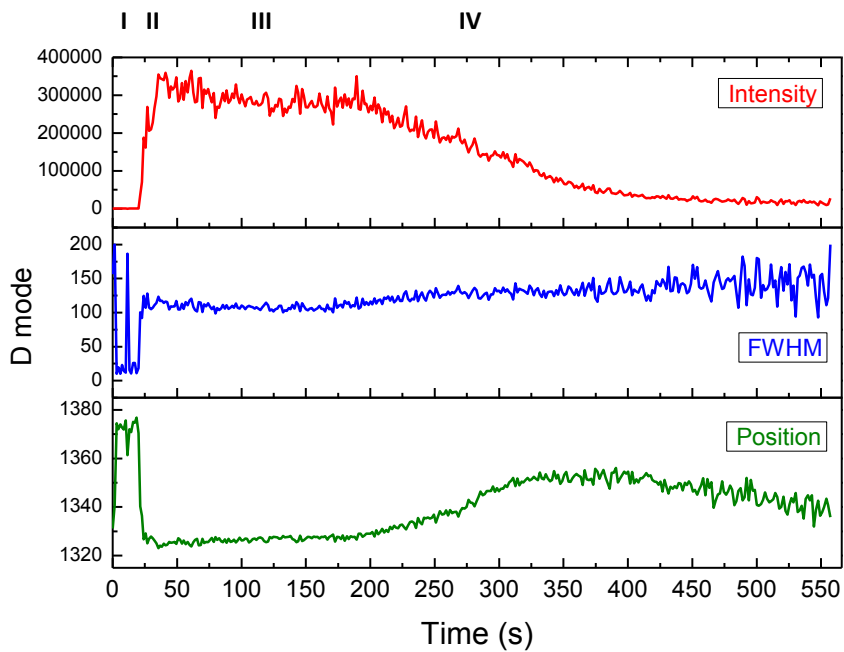


Fig. 4.7. Comparison of the time dependence of the intensity, FWHM, and position of the D mode.

G mode

Here we concentrate on the G peak. The G peak is always present for any carbon material at any excitation energy and it is the most informative peak in many cases [60]. Figures 4.8, 4.9 and 4.10 display the time dependence of the G peak intensity, position and FWHM, respectively. Here again we can mention about four stages as in the D mode case. The intensity initially exhibits a slight drop during the first ~20 seconds. Then a very sharp increase is observed as in the previous case (see Fig. 4.4). The peak traverses local maxima at

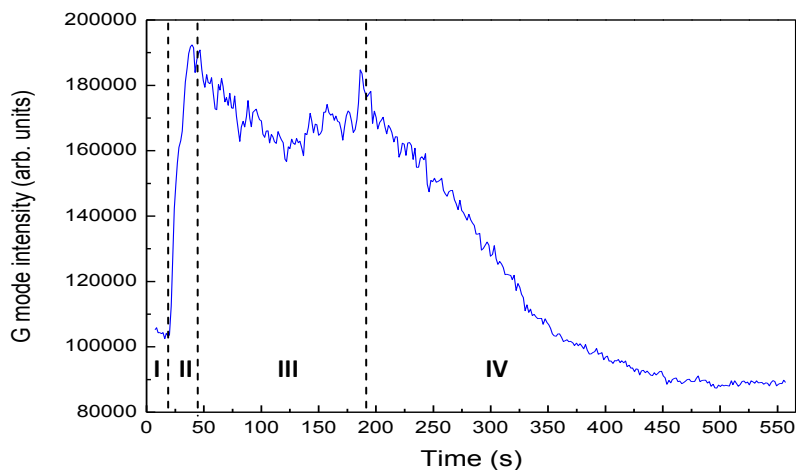


Fig. 4.8. Time evolution of G mode intensity.

around $t = \sim 40$ s. In the third stage the G mode undergoes a decrease and an increase but the intensity values does not vary too much. After the $t = 185$ s, the intensity steadily decreases and eventually becomes constant. The final value is lower than the initial value, which means that the G mode intensity has decreased in overall process during the laser exposure.

In the position versus time graph the G peak first appears at around 1577.5 cm^{-1} in the first ~19 seconds. It continues with a downshift by $\sim 2 \text{ cm}^{-1}$ in the next 2 seconds. Then it remains more or less constant between $t = 37$ s and $t = 170$ s. In the final stage the position increases constantly till 1585 cm^{-1} , which corresponds to $\sim 8 \text{ cm}^{-1}$ upshift from the initial value. This

value is more or less the same for other two modified areas except for the fourth point which has an overall upshift of 10 cm^{-1} .

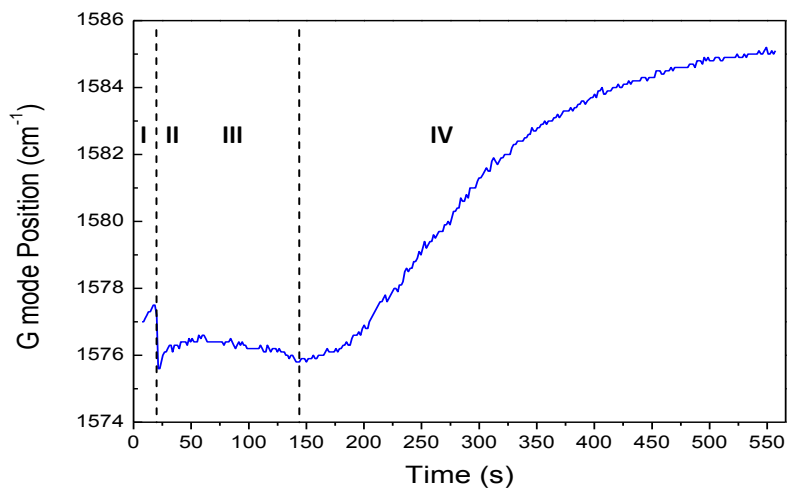


Fig. 4.9. Time evolution of G mode position.

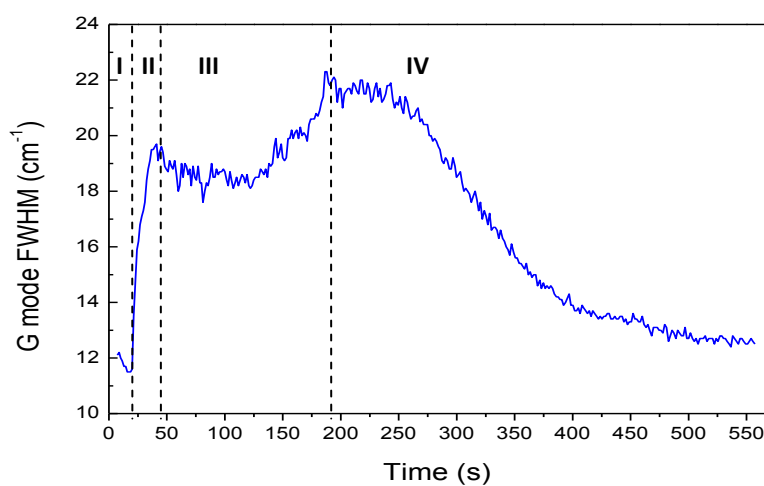


Fig. 4.10. Time evolution of G mode FWHM.

The FWHM vs. time graph of the G mode strangely looks like the intensity graph. They follow almost the same trajectory as can be seen clearly from the Fig. 4.11. Since we use the integrated area under the G peak as an intensity, it is unavoidable to think that the change in the intensity of the G peak is mainly related to the change in its line width.

Fig. 4.11 shows the three peaks of the G mode in one graph in order to compare the time dependence of the changes.

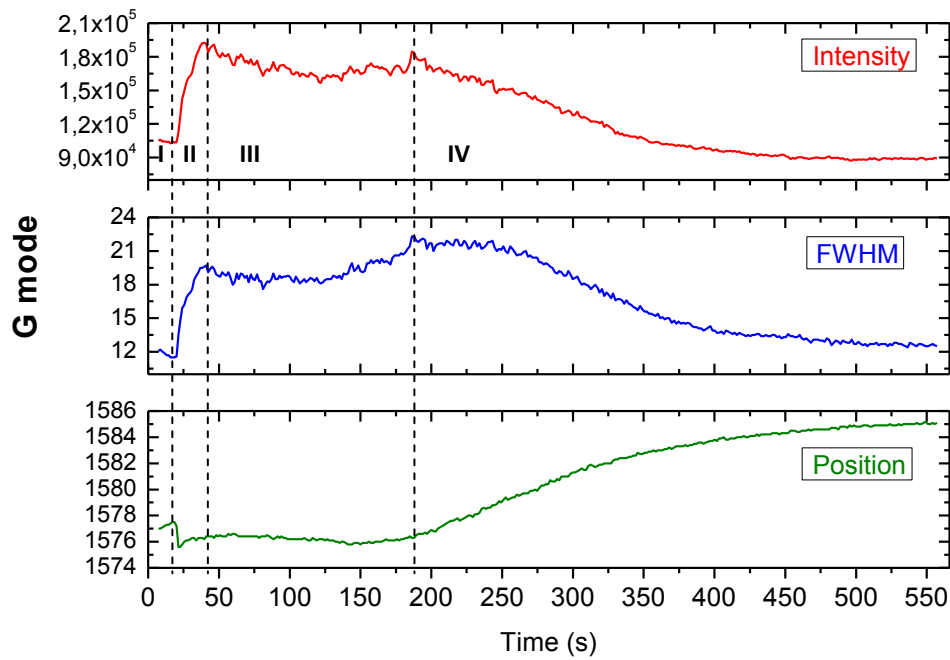


Fig. 4.11. Comparison of the time dependence of the intensity, FWHM, and position of the G mode.

2D mode

The following three figures (4.12, 4.13, and 4.14) depict the time dependence of intensity, position and FWHM of the 2D mode, respectively.

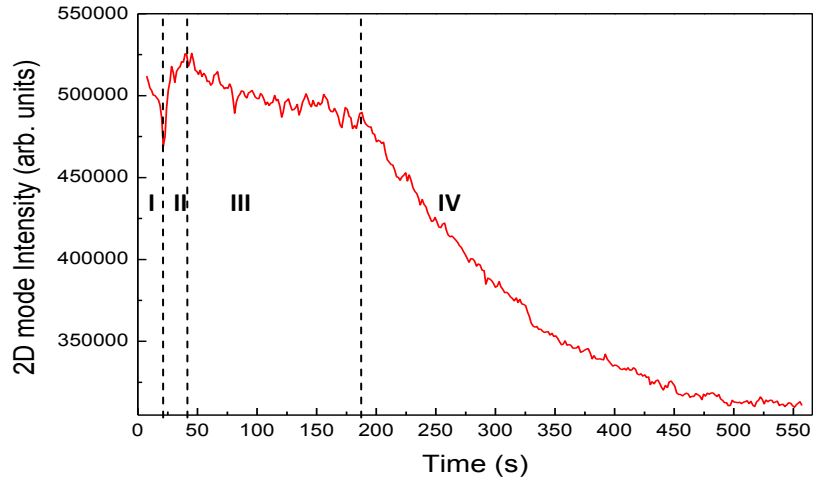


Fig. 4.12. Time evolution of the 2D mode intensity.

Here again we can divide the graph into four stages. Initially the intensity exhibits a rapid drop. It traverses a local minima at around $t \approx 21$ s and then the location of the G mode rises till $t \approx 40$ s. Then it saturates and stays constant with slight decrease till $t \approx 185$ s. and eventually decreases monotonously. However unlike the D and G modes, the intensity of the 2D mode has remarkably decreased compared to its initial value (almost one third of its initial value).

The position versus time graph of the 2D mode is shown in Fig. 4.13. The peak appears at 2658 cm^{-1} . During the first ~ 19 seconds there a very slight upshift by $\sim 0.7 \text{ cm}^{-1}$. In the next 5 seconds a downshift occurs by 1.4 cm^{-1} . At $t \approx 38$ s, the peak undergoes an upshift by 2.7 cm^{-1} . The maximum value of the 2D mode upshift is $\sim 2660 \text{ cm}^{-1}$, which occurs at $t \approx 123$ s. The following decrease continues till $\sim 2658 \text{ cm}^{-1}$ corresponding to $t \approx 187$ s. At the final stage the position does not change significantly and its value lies between 2657.7 and 2658.2 cm^{-1} , which is almost same as the initial value. The results shows that, unlike the G mode, the position of the 2D mode changes only slightly during the whole process.

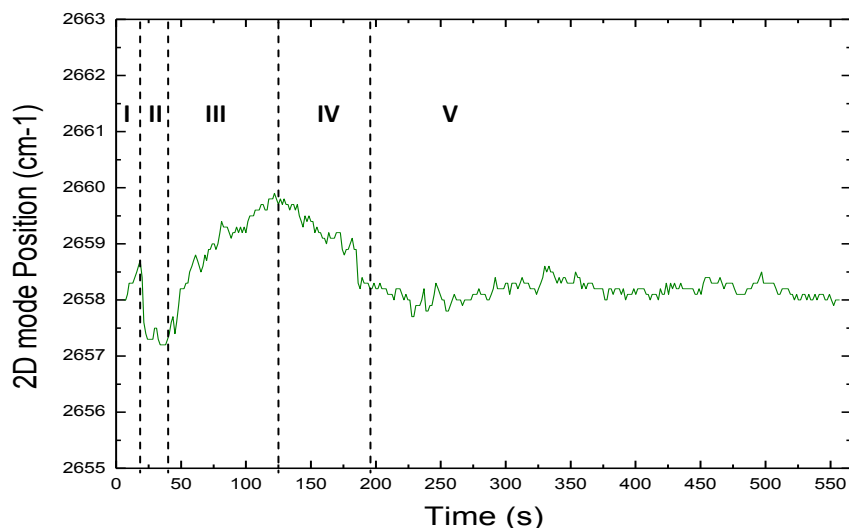


Fig. 4.13. Time evolution of the 2D mode position.

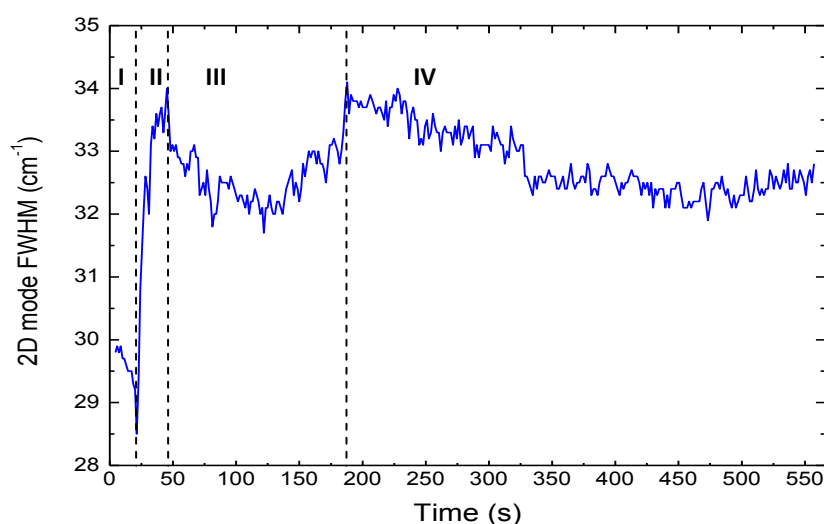


Fig. 4.14. Time evolution of the 2D mode FWHM.

The FWHM vs. time graph of the 2D mode (Fig. 4.14) exhibits a slight drop at the beginning. After $t \approx 21$ s. the peak broadens by 5 cm^{-1} till $t \approx 43$ s. Then the line width decreases again till $t \approx 123$ s. by 2 cm^{-1} and increases again by 2 cm^{-1} till $t \approx 187$ s. It seems that the position and line width of the 2D mode undergo the same time interval at this stage. At the final stage the FWHM decreases slightly and saturates at a value of 32.5 cm^{-1} .

Here again the three 2D mode graphs are included in order to compare the time-dependent changes (Fig. 4.15).

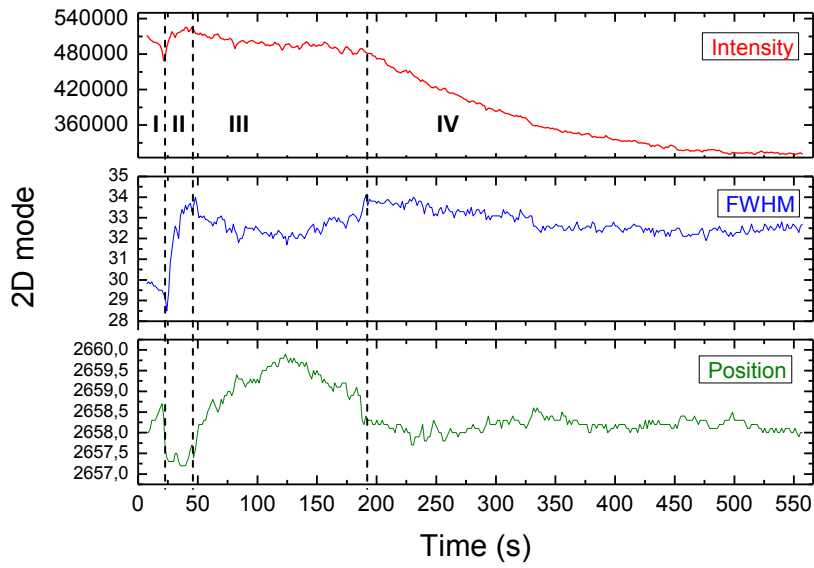


Fig. 4.15. Comparison of the time dependence of the intensity, FWHM, and position of the 2D mode.

Photoluminescence Background

Finally we present the time evolution of the background intensity during the irradiation process in the Fig. 4.16. The spectra was fitted by Python script by choosing a spectral range from 1900 to 2100 cm^{-1} where no obvious peaks are observed. The script can be seen in Appendix A. This kind of fluorescence behavior is not very common in the Raman spectrum of graphene.

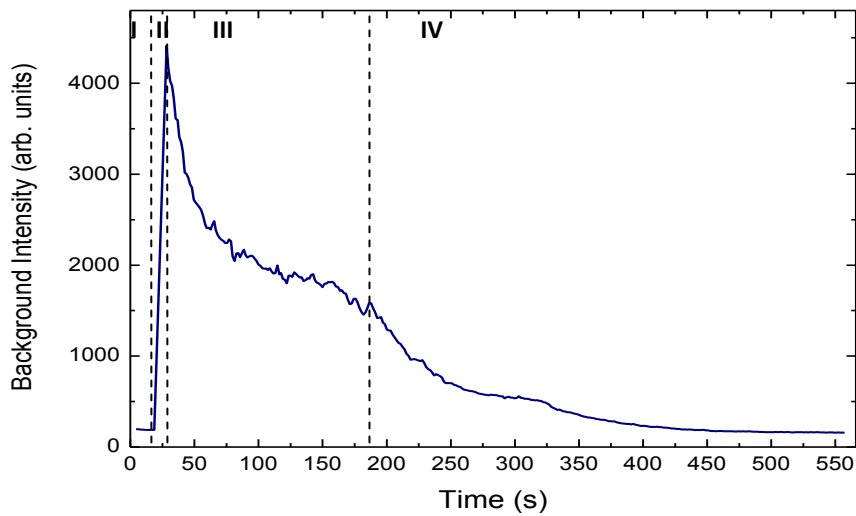


Fig. 4.16. Time dependence of the background intensity.

The background is not observed till $t \approx 19$ s. Then it increases dramatically in the next ~ 10 seconds followed by decrease. There is a saturation process between the time intervals $t \approx 120$ and $t \approx 185$ s. , which then continues with a monotonous decrease until it disappears.

Considering all these results presented so far, we will argue that there are mainly three processes that can account for the spectral changes.

Firstly, in our spectrum we observe very broad D and G modes similar to amorphous carbon. The laser-induced heating can be held responsible for carbonization of hydrocarbons on the surface of graphene originating from polymeric adhesive residues. These adhesive residues are present on the graphene layer as a result of micro-mechanical exfoliation process [66, 67].

A typical signature of C-H bonds in visible Raman is the increasing photoluminescence background for increasing amount of H content [47]. We observe a strong background in our measurements, which implies that the laser-induced decomposition of polymer residues can be the source of photoluminescence background in our spectrum.

Secondly, the environmental oxygen molecules are thought to be one of the key factors in removal of a-C under high temperature and ambient conditions. Besides that, photo-oxidation is assumed to be the main factor in doping of the graphene sample.

Thirdly, the behavior of the G peak such as broadening and upshift together with the presence of the D mode indicate an increase in the number of broken sp^2 carbon-carbon bonds which results in a nanocrystallization of graphene. It is interesting to note here that after the laser irradiation experiment, a mapping Raman measurement shows a significant D mode under the laser spot. We associate this D mode with the adsorption of additional molecules from ambient air when the laser is turned off.

The following figure shows the Raman spectra of single layer graphene with the highest D mode intensity under laser irradiation. The data was fitted by Origin 8. We observe a broad G peak here (for clear view see Fig. 4.3a). The spectrum around 1600 cm^{-1} can be decomposed into three different peaks. The pink colored peak is the well-known D' mode which is due to the defect formation. The most intense peak at the middle is the G peak of SLG. The other peak is assumed to originate from amorphous carbon. A Raman spectrum of carbon black is shown in the Fig. 4.18 for the comparison.

Recently it was suggested that the scotch tape residues contaminate the graphene surface at elevated temperatures [66, 67, 70]. These polymeric hydrocarbon residues are thought to be

the source of amorphous carbon. Under the elevated temperature the carbonization of hydrocarbons occur. It is important to note that we did also the same Raman experiment on the bare substrate and we did not observe any broad Raman peaks. This indicates that the carbonization of tape residues occurs particularly on the graphene surface.

If we take this assumption into account we could explain the behavior of the D mode intensity during the laser treatment. The first stage is the threshold stage, where the temperature increases. When the temperature is high enough, the photodecomposition of the tape residues starts. This results in contamination of graphene layer. C-H bonds are broken. Carbonization and hydrogenation are the possible processes. The observed strong background can be attributed to the hydrogenated carbon and the broad peaks at the beginning can be due to the amorphous carbon resulting from carbonization of hydrocarbons. When the process is finished the D mode saturates, but as the irradiation continues the amorphous carbon is eventually removed from the graphene surface as a result of destructive photo-oxidation. The disappearance of the broad D and G modes can be explained with the removal of amorphous carbon.

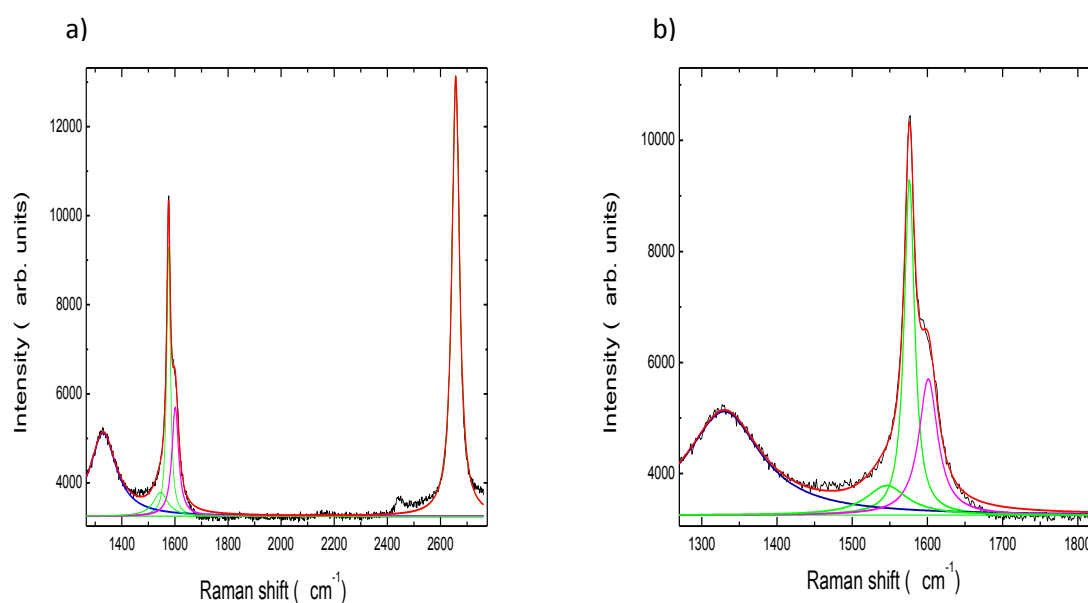


Fig. 4.17. a) Raman spectrum of exfoliated SLG after 41 seconds irradiation with 532 nm laser at 33 mW power. The D peak is fitted with a single Lorentzian (blue) for D_{ac} , and the G peak is fitted with two Lorentzians (green) centered at 1543 and 1576 cm^{-1} . The former G_{ac} peak is associated with amorphous carbons, whereas the latter belongs to graphene itself. The pink colored peak at 1601 cm^{-1} shows the D' mode. The 2D peak is fitted with a single Lorentzian. b) expanded view of (a)

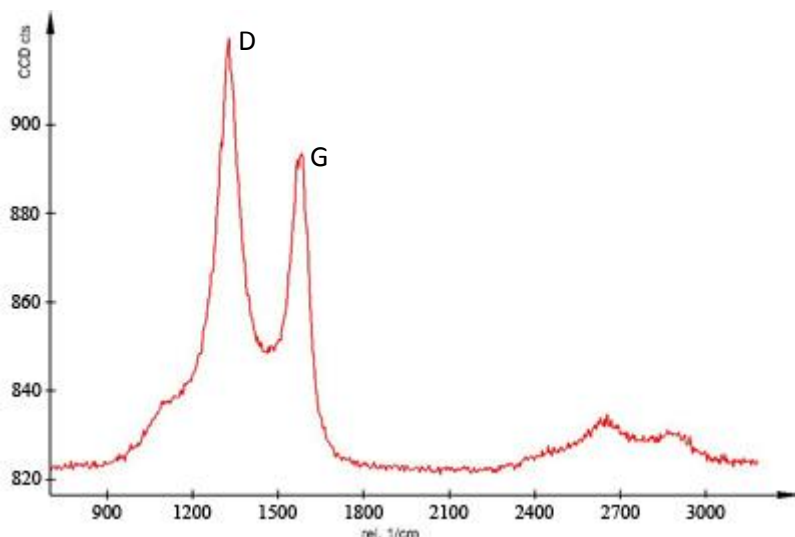


Fig. 4.18. Raman spectrum of commercial carbon black. (taken from Ref. [71])

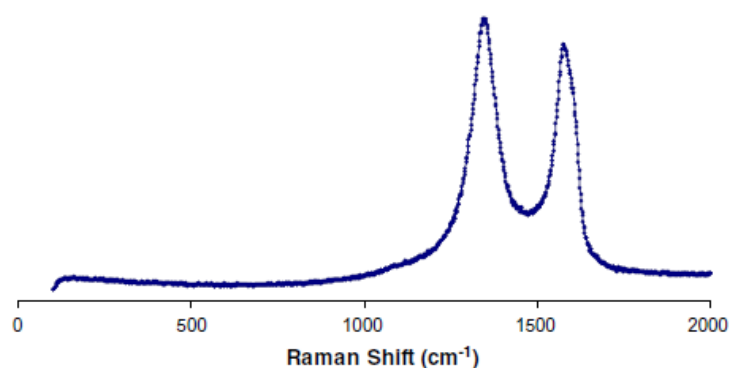


Fig. 4.19. Raman spectrum of reduced graphite oxide (GO) (taken from Ref. [72])

Another possible explanation for the spectral changes could be the photo-induced oxidation of graphene. The evolution of the spectra at the first two stages is very similar to that of graphite oxide shown and disordered graphene shown in Fig. 4.19. This explanation suggests that the sp^2 carbon network of graphene has been broken into nanometer sized domains, i.e., nanocrystallites [39]. In one of the papers, the decrease in the D and G band intensities at the later stages is attributed to the photo-oxidation of severely damaged carbon network [19].

It was mentioned before that the G mode intensity is proportional with the amount of carbon atoms. In our spectra (see Fig. 4.8) the G peak shows a dramatic increase at the second stage. This means that the amount of carbon atoms is increased. The only source of the carbon in this case can be the polymeric adhesive residues on the graphene surface. We also noted that the G mode FWHM and intensity follow a very similar trajectory in time resolved measurement. Since we measure the area under the G peak as an intensity, the change in the

FWHM will change the intensity of the G peak. It can be concluded here that, it is mainly the FWHM of the G peak that undergoes a change, and not the G peak amplitude. The new broad peaks around the G mode causes the FWHM to change and consequently the intensity of the G mode changes.

On the other hand, the G peak FWHM is a measure of disorder and increases continuously with increasing disorder [60]. In our case the FWHM of G mode increases in the first three stages and decreases at the final stage. It is important to note here that the increase of G peak line width could also be due to combination with the new arising peaks originating from the amorphous carbon.

The position of the G peak is very sensitive to dopants. An increase in the G peak is an indication of p-typed doping. The laser is believed to destroy some sp^2 C-C bonds and gradually decompose the single-crystal graphene into a nanocrystalline structure [17]. In the

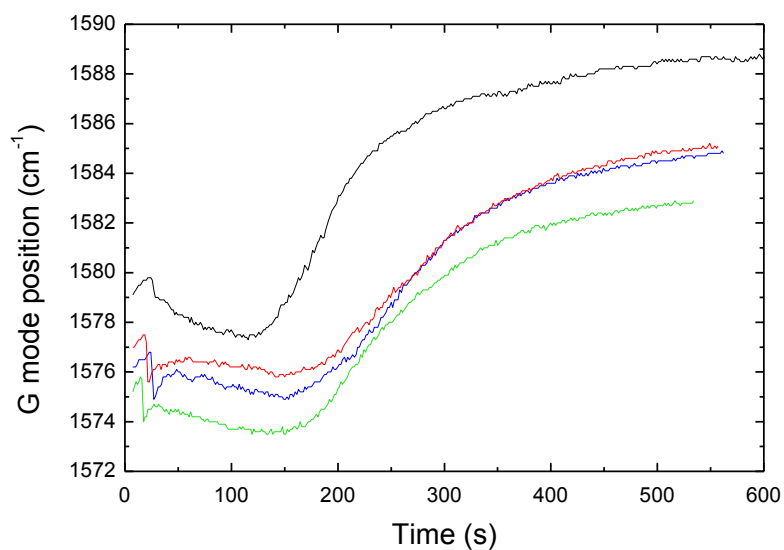


Fig. 4.20. The G peak position of four different laser-irradiated areas on an SLG sample.

amorphization trajectory introduced by Ferrari and Robertson, during the nanocrystallization of graphene, the G mode moves to higher values which matches with our results. The following Fig.4.20 illustrates the increase in position of the G peak of four different laser-irradiated points on our SLG sample. All the peaks show similar upshifts in their position.

As mentioned in the second section, the G mode position ($Pos(G)$) upshifts under both electron and hole doping (*see Fig. 2.10 (b)*) [49]. The increase in the $Pos(G)$ can be up to 30 cm^{-1} for hole doping and 25 cm^{-1} for electron doping [49]. The results in the literature report

that the FWHM of the G mode decreases under the both type of doping (see Fig. 2.10 (c)) [49]. Moreover, the 2D and G bands show very different dependencies on the doping. As shown in Fig. 2.10 (c) the position of the 2D mode does not change much for electron doping except for the higher gate voltages ($> \sim 3$ V) [49]. In our experiments the 2D mode position upshifts slightly at the third and fourth stages (Fig. 4.13).

The G mode upshift together with 2D mode upshift is a sign of charge carrier doping and generally interpreted as evidence of oxide doping [73].

Intensity ratios of *D*, *G*, and *2D* modes

The ratio of *D* and *G* peak intensities I_D/I_G is commonly used to quantify the defect density [59]. Fig.4.21 shows the evolution of this ratio during the laser irradiation. Initially the ratio is zero since there is no *D* mode. After first 23 seconds of irradiation, the ratio I_D/I_G increases

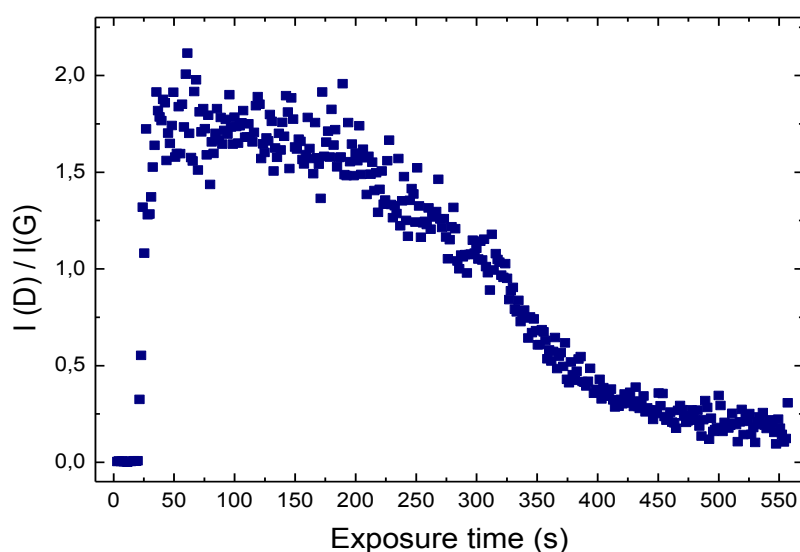


Fig. 4.21. The I_D/I_G ratio as a function of irradiation time at 532 nm.

rapidly, attains its maximum, stays in equilibrium for some time and then falls monotonously. The continuation of the irradiation results in a slower decrease or saturation of the ratio. The trends summarized by the amorphization trajectory proposed by Ferrari and Robertson for carbon materials indicate that I_D/I_G increases when crystalline graphite transforms into nanocrystalline graphite and then decreases when nc graphite becomes mainly sp^2 amorphous

carbon. Based on the reported data, our case seems to follow the first two stages of the amorphization trajectory. It suggests that crystalline graphene under laser irradiation transforms into nc graphene and then, as the radiation damage increases, becomes more disordered which corresponds to amorphous phase.

However, as mentioned before according to amorphization trajectory, the G peak position decreases as the nc graphite evolves into an amorphous phase. In our case we observe an upshift in the G mode position which saturates after some time. This trend was observed in all samples even under longer exposure time (~45 minutes). Due to this fact, we believe that graphene is still in the first stage and it does not evolve into sp^2 amorphous carbon. Besides that, if the graphene would contain such amount of disorder, it could not be observed such a regular and sharp $2D$ mode in the Raman spectrum.

The crystallite size can be determined by using the TK relationship mentioned in the section 2.2.5. Here, we could conclude from the I_D/I_G ratio that the nanocrystallites have a characteristic average size of approximately 7-8 nm. Since we believe that graphene does not undergo the

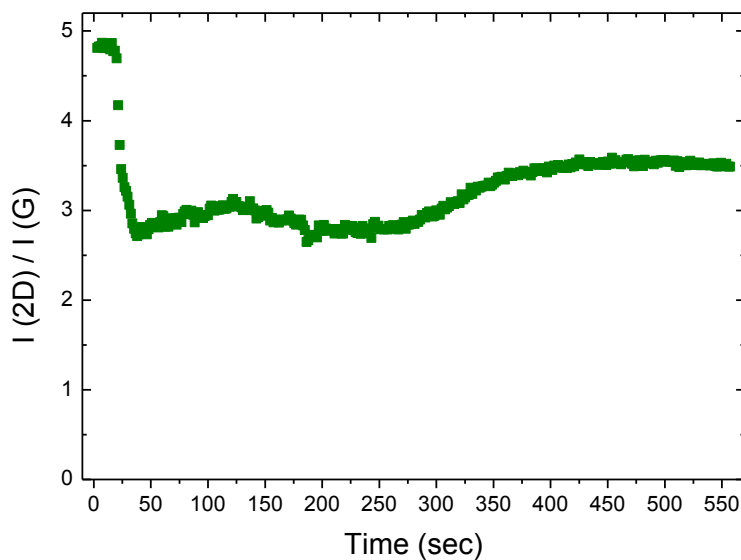


Fig. 4.22. The ratio of I_{2D}/I_G versus time at 532 nm.

third stage of amorphization trajectory, it is reasonable to state that after the (I_D/I_G) ratio reaches its maximum, the bond-breaking process terminates and the crystallite size stays at an average value of 7-8 nm.

Here, the bond breaking process could be induced by two photon processes, since the energy of a single photon is smaller than the binding energy of carbon atoms [17]. Another possibility is that, photo-induced chemical reactions between graphene and ambient molecules such as oxygen, H₂O, polymeric residues and substrate could be responsible for the bond breaking mechanism.

The intensity ratios of the 2D and G peaks show a strong dependence on dopants, which makes it a sensitive parameter to monitor the level of doping [49]. The Fig. 4.22 plots the ratio I_{2D}/I_G as a function of exposure time. At the first stage the ratio is constant, whereas in the second stage it drops dramatically. Third stage continues with slight increase and decrease. At the final stage the ratio increases slightly and saturates. The final ratio of the 2D and G peak intensities is approximately 3.5. Strangely, this value corresponds to pristine graphene which is ~3.4. Fig. 4.23 (a) plots the I_{2D}/I_G as a function of Pos(G). Here our results does not match very much with the results reported in Ref. [36]. However, it is important to note that here the G mode intensity is strongly affected by the crystallite size and the ratio I_{2D}/I_G serves no longer as a measure of doping [17]. Due to this fact it is difficult to distinguish the doping effects from the other factors affecting the Raman spectra.

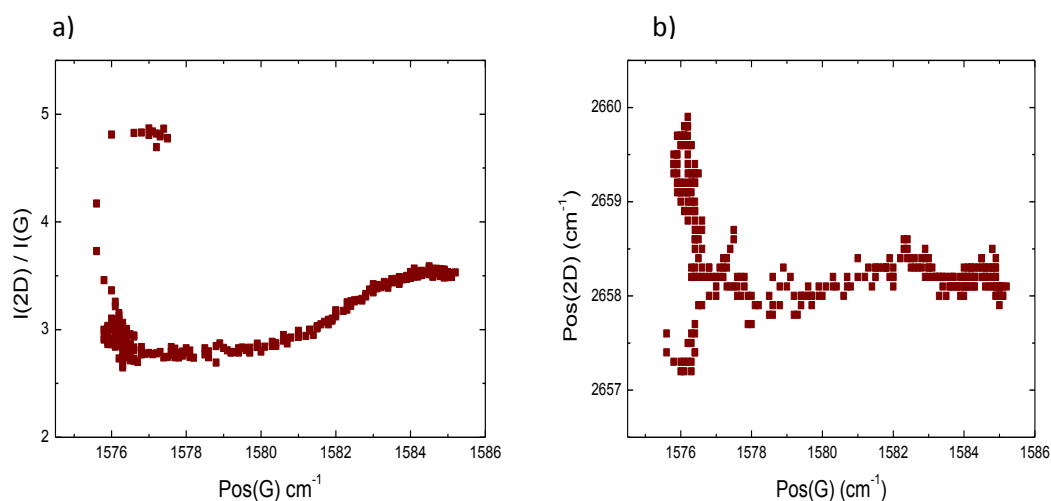


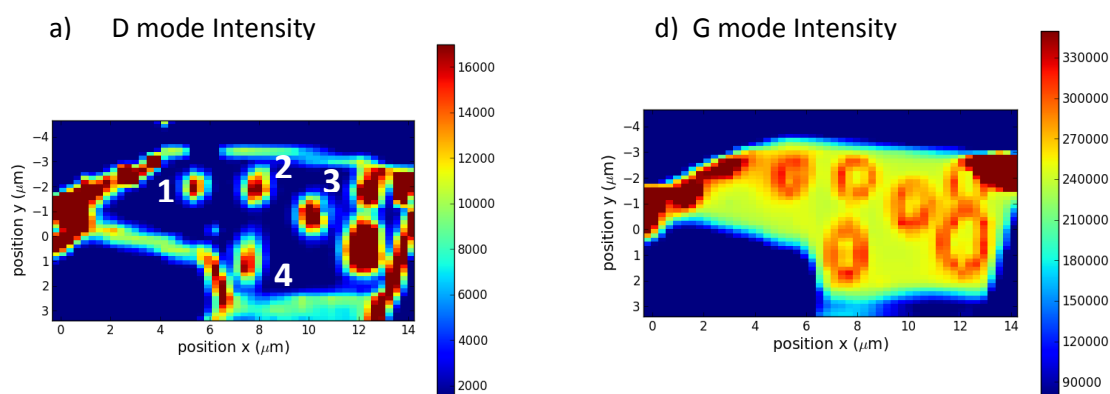
Fig. 4.23. a) I_{2D}/I_G as a function of G peak position b) 2D Peak position as a function of G peak position

Fig. 4.23 (b) correlates Pos(2D) and Pos(G). Here the first part of the graphs is very complicated which might be due to multiple effects playing role on the change of these parameter (which is also the case for Fig. 4.23 (a)). After the equilibrium is reached we

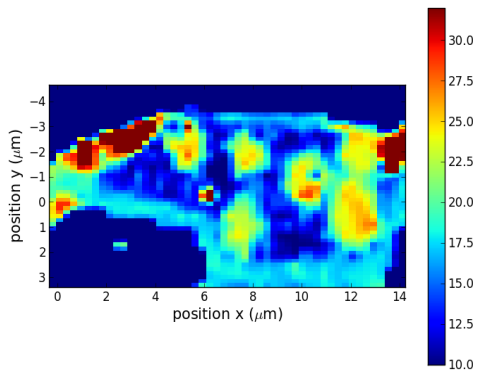
observe that the 2D mode changes very slightly ($\sim 1 \text{ cm}^{-1}$), whereas Pos(G) increases. Compared with the results presented in Ref. [49] (Fig. 2.10 (b) and (d)), we can conclude that this is a n-type doping. However, if we attribute the increase in the G peak position to the nanocrystallization, this conclusion does not hold any more. Besides that, the possible surrounding molecules (e.g., O_2 , water) transfer charge and act as a p-type dopants on graphene [17]. This p-type doping was reported in transport experiments of Ref. [17].

4.1.3. Raman mapping measurements

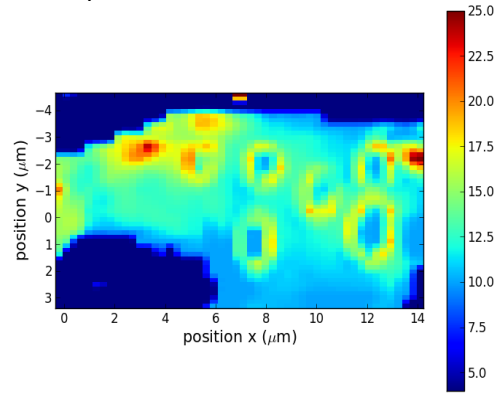
The Raman mapping involves the coordinated measurement of Raman spectra with successive movements of the sample by a specified distance [74]. The Raman image is a chemical contour map which is based upon an intensity based color scale. We performed the Raman mapping on single-layer graphene flake after the laser irradiation. Fig. 4.24 shows the results of the Raman mapping measurements. Here the spatial maps of intensities, line widths, and peak positions for each of the D, G, and 2D peaks are given separately. The Raman spectrum was recorded for each location with a step size of 250 nm in both spatial directions at 2.33 V laser energy. The spectrum was fitted by the Python script which can be seen in Appendix A. The images were processed and viewed by contour plot script written in Python.



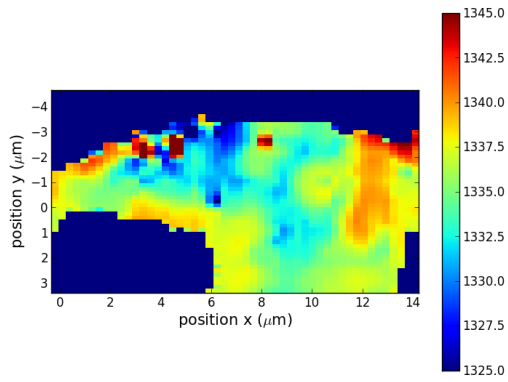
b) D mode FWHM



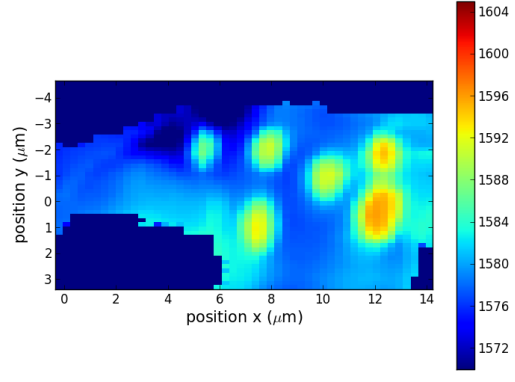
e) G mode FWHM



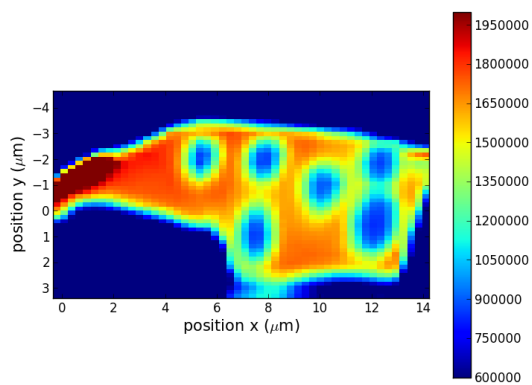
c) D mode Position



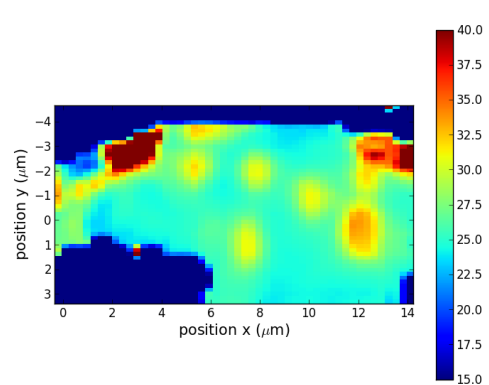
f) G mode Position



g) 2D mode Intensity



h) 2D mode FWHM



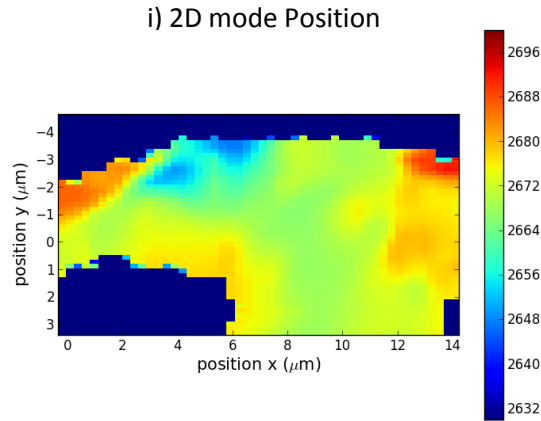


Fig. 4.24. a) Intensity map of the D mode. The numbers indicate the modified points of interest. b) FWHM map of the D mode c) Position map of the D mode d) Intensity map of the G mode e) FWHM map of the G mode f) Position map of the G mode g) Intensity map of the 2D mode h) FWHM map of the 2D mode i) Position map of the 2D mode. The spatial resolution of the Raman maps is 400 nm. The Raman images are based on the peak-fitted parameters.

From these results we see that the laser caused substantial changes on the Raman spectra of graphene. The D mode is clearly observed in the Fig. 4.24 (a). In previous section we mentioned that the D mode intensity decreases to its initial value at the end of the process (see Fig. 4.4), however when we zoom in the D mode region of the initial and final spectrum we can see the small difference as shown in Fig. 4.24. Still it is a question that why we do not observe a distinctive D mode at the final spectra and why the D mode decreases after such a dramatic increase.

The Raman spatial images also reveal some distinctive aspects of the laser-modified regions. The D, G, and 2D mode intensities show remarkable phase changes along the diameter of the

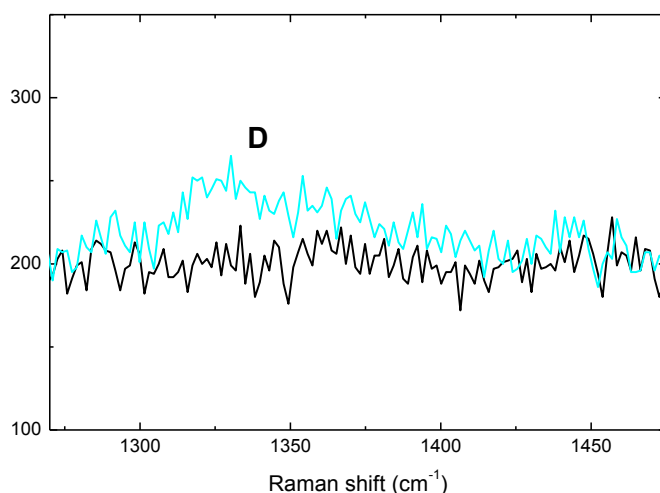


Fig. 4.25. The magnified image of the D mode intensity before and after the laser irradiation. Spectrum belong to the second modified area. The black colored spectra is the initial spectra.

circular modified region. At the center of the modified region we observe a more defected area with decreased 2D mode intensity and relatively intense D mode. Around this region there is a ring shaped area which is less affected and/or has a different chemical composition. The outer border of this ring also shows different results. This is probably because of the Gaussian distribution of the laser beam on the SLG flake. The intensity of the laser is higher at the center and becomes weaker as it moves away from the center.

4.1.4 Atomic Force Microscopy

The affected region can be observed more accurately by recording the topography with AFM. Here we present the AFM images of the sample obtained after the laser treatment which we discuss here. These images were taken a few days after the laser exposure. The measurements were performed in a non-contact mode. Fig. 4.26 (a), (b), (c), (d) and (e) depict the 2D and 3D AFM images of the monolayer graphene with different magnifications. Fig. 4.27 (b) and (d) are the height scans along the light blue lines drawn in Fig.4.27 (a) and (c), respectively. Fig. 4.26 (a) shows the four affected regions, numbered with respect to the experimental sequence. The diameter of the modified area is almost the same for all four points with a value of $\sim 1.4 \mu\text{m}$. This value is nearly twice of the laser spot size ($\approx 740 \text{ nm}$). The measured height of the non-affected region where we are supposed to have normal graphene is $\sim 0.8 \text{ nm}$ instead of

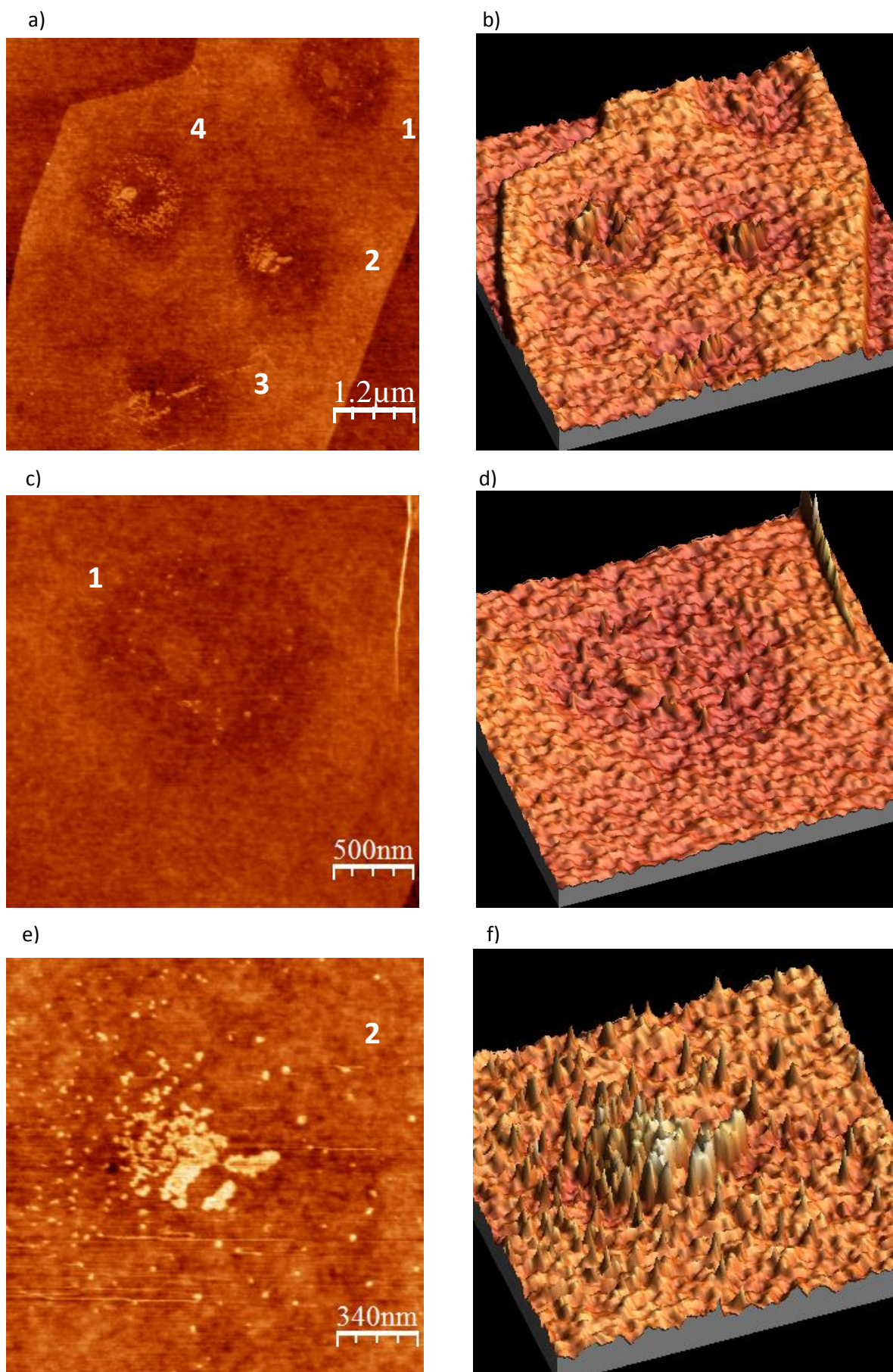


Fig. 4.26. (a), (c), and (e) AFM topographical images of SLG at different magnifications exposed to laser at 532 nm. (b), (d), and (f) 3D AFM images of (a), (c), and (e), respectively.

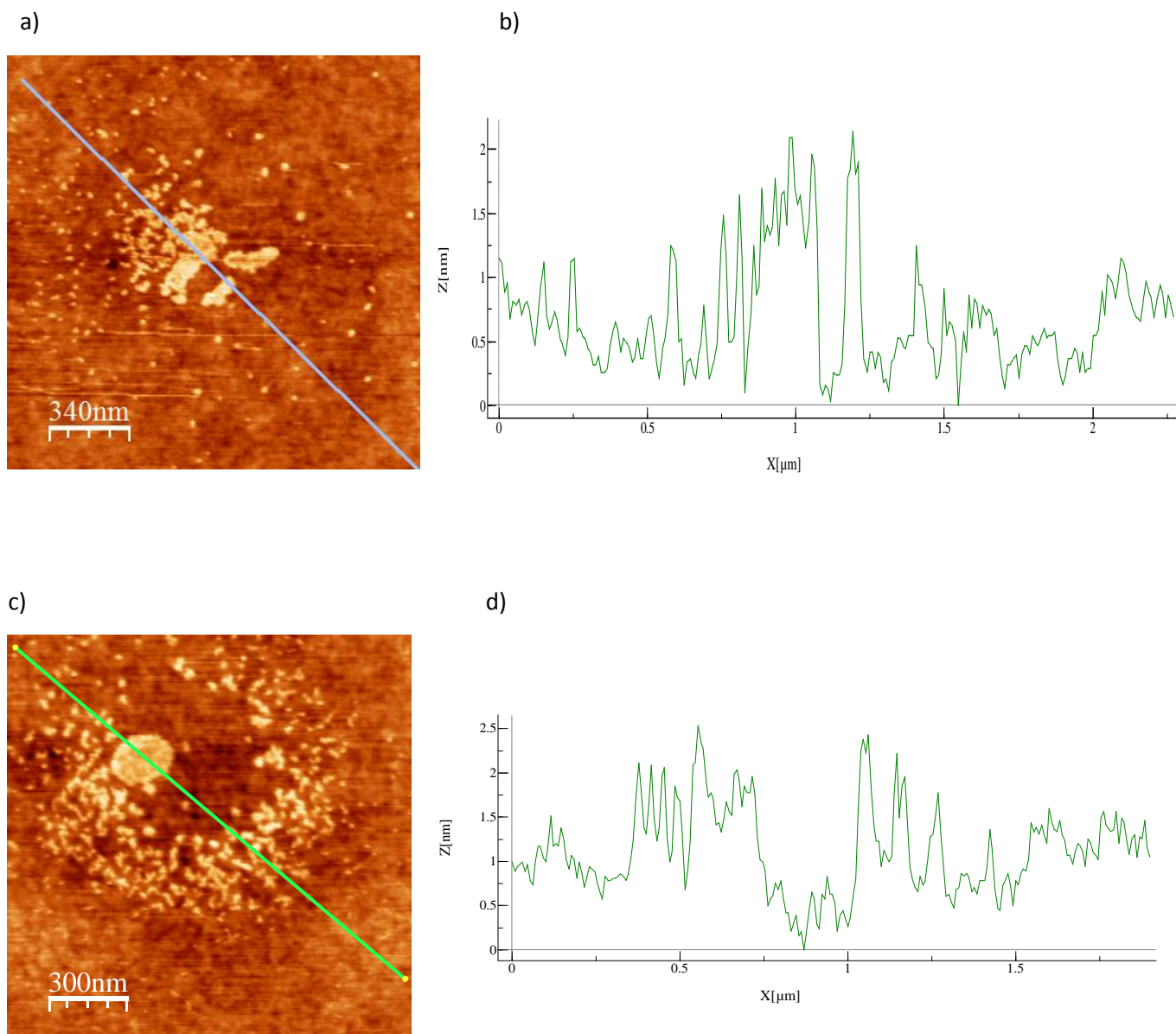


Fig. 4.27. (a) and (c) AFM topographical images of second and fourth regions, respectively (b) and (d) height profile scans along the line shown in (a) and (c), respectively.

~0.34 nm as expected for monolayer. This height difference has been reported previously and is attributed to adsorbed molecules on top of the graphene surface and/or the molecules in between the graphene layer and the substrate [75]. In the modified regions the height is decreased to approximately 0.4 nm. This might be due to the removal of adsorbates as a result of laser heating and/or etching of the substrate under the laser exposure. However, inside of the affected area we observe elevated regions which are shown with bright colors. Especially the second, third, and fourth modified regions show distinctive bumps on their surfaces. The height of these bumps ranges between 1 nm and 1.5 nm. This unknown matter on top of the

graphene surface can be the molecular adsorbates from the ambient air and/or amorphous carbon originating from polymeric residues as mentioned before.

AFM images after heating the sample

In order to understand the nature of this unknown material on top of the graphene surface we decided to heat the sample under the ambient conditions. Heating of the graphene is known as a method to remove the dopants from its surface. It was suggested that if these bumps originate from the adsorbed molecules from the ambient air they should change in shape and size. It is worth noting that the heating experiment was conducted three months after the laser experiment. Therefore before heating the sample, we first performed the AFM experiment to see if there is any change on the flake and if this unknown material has changed in shape. There were no changes on the flake except a few minor differences. Then we heated the substrate on a heating plate at 200 °C for 5 minutes in an open air. Immediately after the heating the sample was placed in the AFM and the images were obtained under the same setup. We observed very surprising results. Fig.4.28 (b) shows the AFM image of the flake after heating. The previous image is also presented for the sake of comparison in (a). One can easily observe the changes on the affected region.

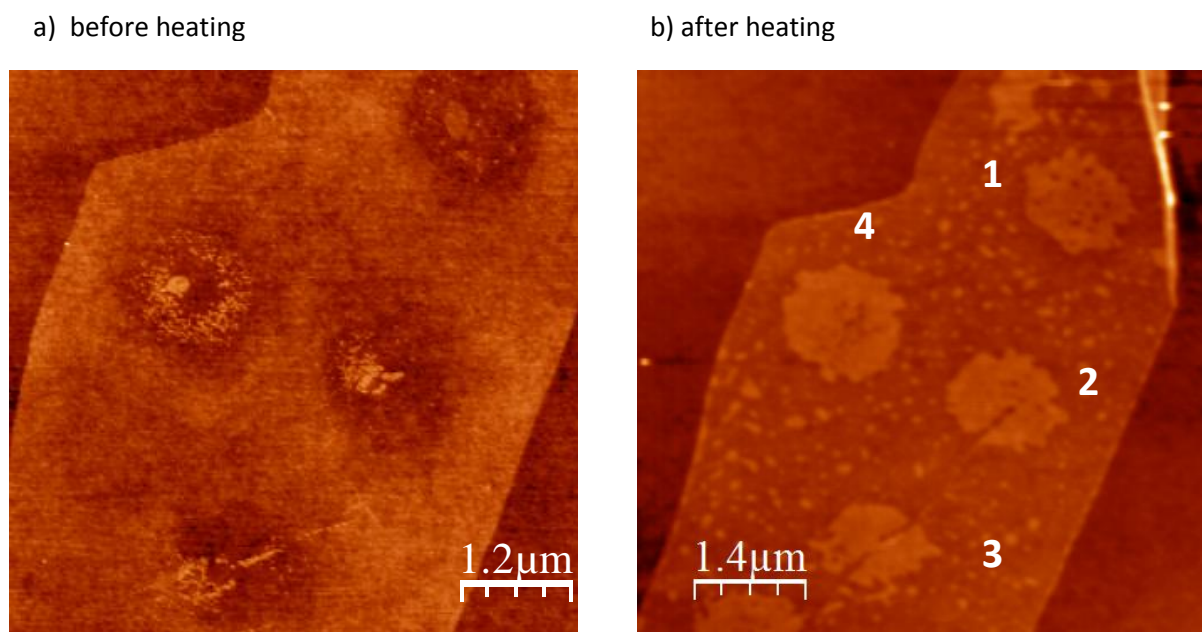


Fig. 4.28. (a) AFM image of the SLG flake before the heating and (b) after heating.

This result was puzzling because if it is the amorphous carbon on top of the graphene surface that causes the height change, why should it increase in amount so distinctively? Or is it due to the air molecules getting into reaction with the laser-affected graphene or amorphous carbon? Is it a nucleation process? Or is it just a doping effect? So far we could not find a satisfactory explanation for this observation. Moreover, it is not only the laser-treated area that is effected, also the graphene around has changed a bit. We observe "foreign particles" all over the graphene flake. The following images are the AFM images of selected affected regions. Fig. 4.30 depicts the height profile of the second point shown in (b) along the line.

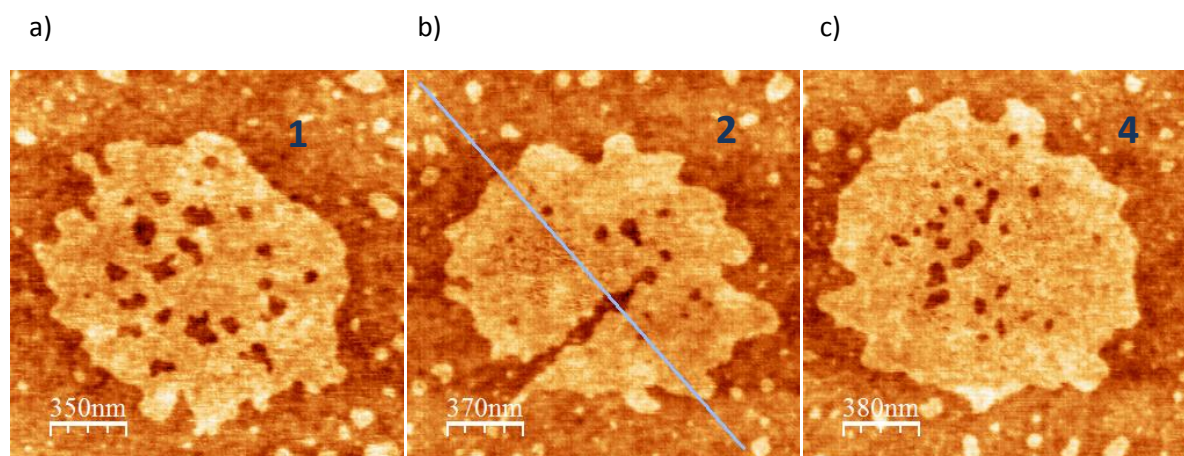


Fig. 4.29. a) AFM image of point 1 b) point 2 and c) point 4.

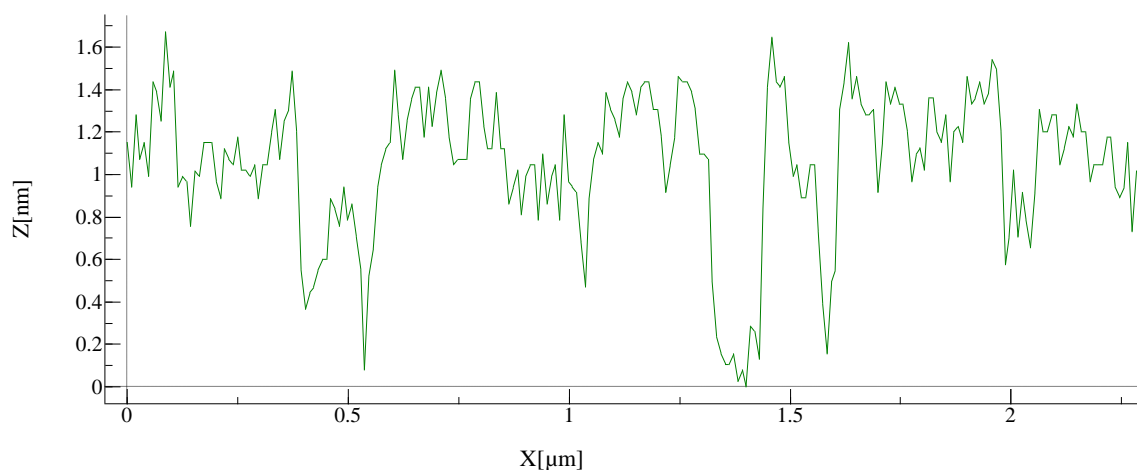


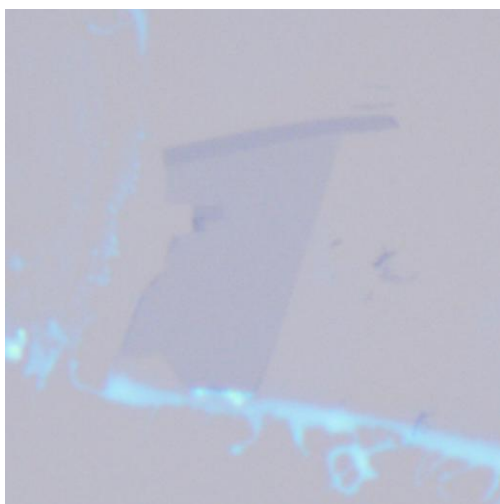
Fig. 4.30. Height analysis of the second modified area across the line scan shown in Fig. 4.29 (b).

4.2. Pulsed Laser Exposure

In this part we will present the results obtained with a different type of laser. This time we have used much powerful pulsed laser to test the monolayer graphene. The details of the experiment are explained in the second chapter.

In this experiment the results differed from the previous one in many aspects. First of all, the damage of the laser is clearly seen even from the optical image as shown in Fig. 4.31. We have to note that the duration of the pulsed-laser exposure was more or less one second whereas in the first experiment it was about 10 minutes. The exposure time was controlled manually by placing a beam stopper between the laser source and the setup. In longer exposure times the damage is extremely destructive such that the large black spots were immediately observed in the optical image (both on substrate and thick graphite flakes). We have irradiated the sample with pulsed laser 12 times and obtained 12 spots. However, in the optical image only 11 of them are observable. This is because in the final case the laser was focused on a silicon substrate. It is found that the damage on the silicon substrate is not observable in a short exposure time ($< \sim 1$ s) in an optical image whereas in longer exposure times it is clearly observed. Fig. 4.32 depicts the AFM images of the same flake. The flake size can be estimated from the AFM image to be $8 \mu\text{m} \times 14 \mu\text{m}$ ($112 \mu\text{m}^2$). Figures 4.33 and 4.34 show two of the laser-irradiated areas and their corresponding height profile images.

a) SLG before exposure to pulsed laser



b) SLG after exposure to pulsed laser

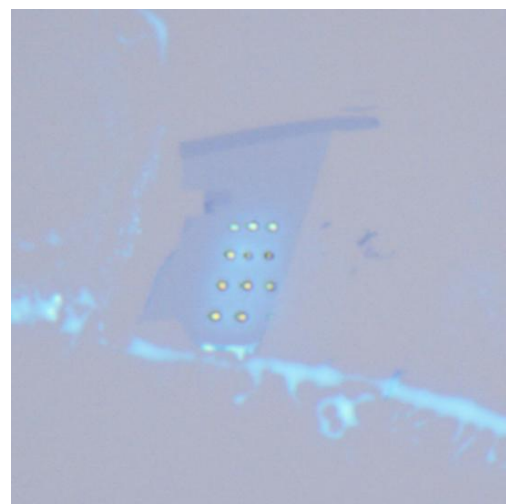


Fig. 4.31. a) SLG flake b) the same flake after the laser exposure (pulsed laser with 370 nm wavelength). One can see the damage clearly.

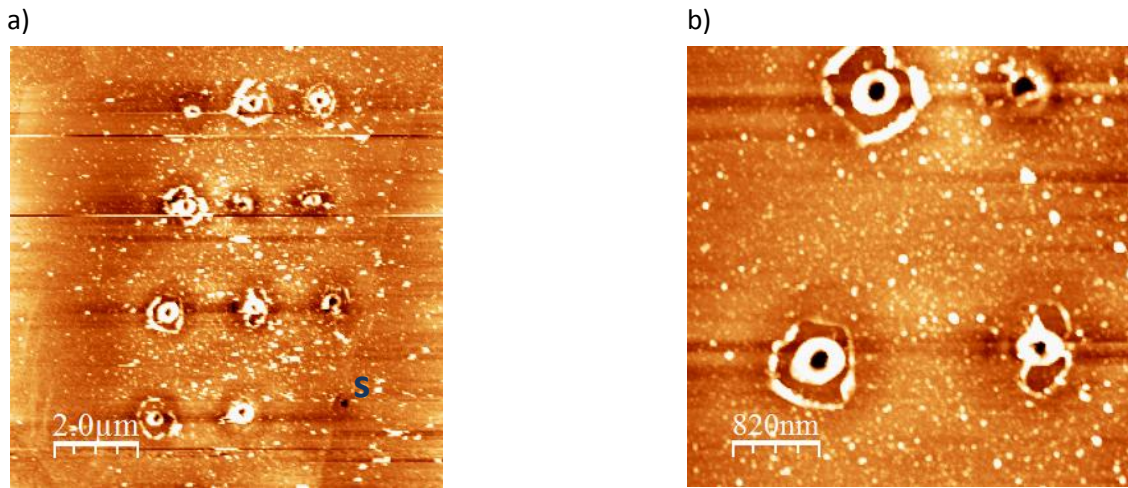


Fig. 4.32. a) AFM image of monolayer graphene after the pulsed-laser irradiation b) AFM image of (a) in a different scale.

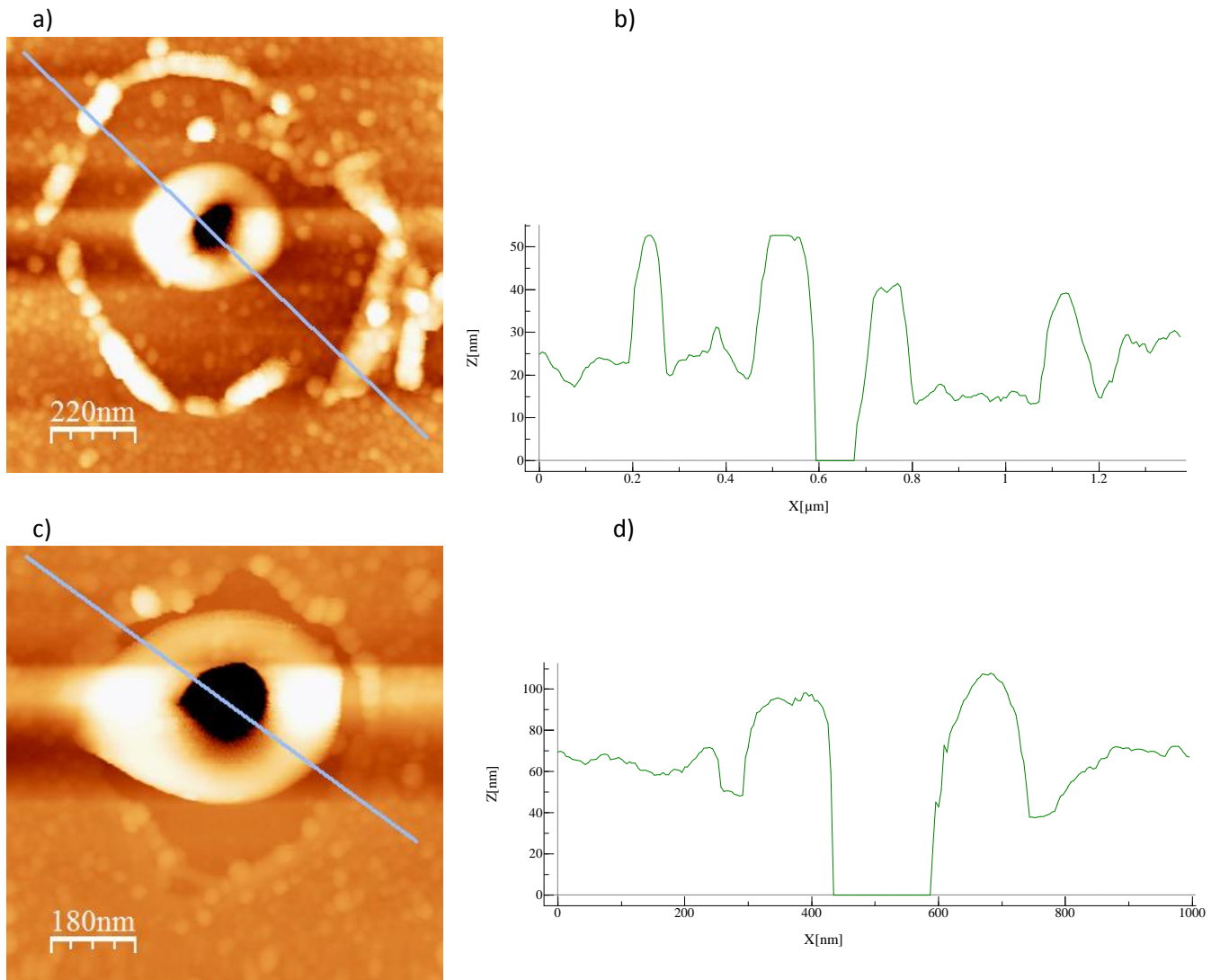


Fig. 4.33. a) and c) Noncontact AFM images of the pulsed laser-affected regions b) and d) corresponding height image across the line shown in (a) and (c), respectively.

In the optical image shown in Fig. 4.31 (b) one can see the nicely patterned spots on the graphene flake. The AFM images of Fig. 4.32 show that the shape and size of the spots induced by the pulsed laser differ from each other. Most probably this was caused by the duration of the laser irradiation. The spot defined with S letter in Fig. 4.32 (a) is located on a Si substrate. This spot looks quite different than other spots. It suggests that the ring shaped structures around the center of the modified regions are caused by graphene. The height images shown in 4.33 (b) and (d) suggest that there is a hole at the center of the spot. The laser has actually also damaged the substrate and the hole seen in the images goes through the substrate. The exact deepness of the hole could not be obtained because the tip of the AFM could not reach the end point. From the height images we can estimate the height of the elevated region to be ~ 25 nm which is much higher than the values measured in the previous experiment (~ 2 nm). Obviously, here we have a different situation and much stronger damage compared to the previous case. Considering these observations we conclude that the Si/SiO₂ was melted under the pulsed-laser irradiation as a result of laser-induced heating and the melted part of the substrate has moved out of its surface. This can also be predicted from the following Fig. 4.34 which shows the 2D and 3D AFM images of the hole induced by the pulsed laser. It should be noted that these images were taken several days after the sample was treated with the pulsed laser which means that the sample was already cooled down.

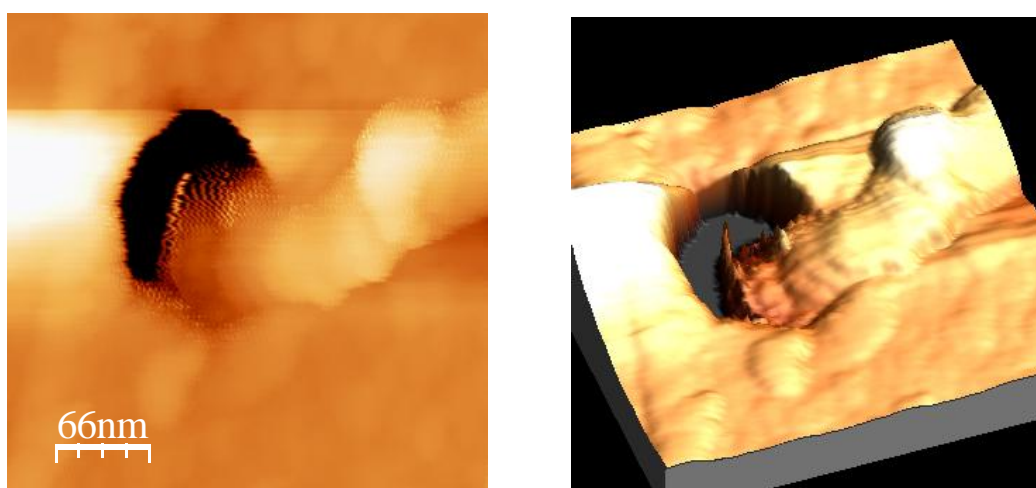


Fig. 4.34. a) Noncontact mode AFM image the hole opened in graphene and Si/SiO₂ surface b) The 3D image of the (a).

In the case of substrate there is no elevated region around the hole which can be interpreted as the evaporation of the substrate under the pulsed laser exposure due to laser heating. However in case of graphene the melted substrate seems to be in contact with graphene. Based on these results, we propose such an explanation that, when the laser is focused directly on the substrate, the substrate under the laser irradiation melts down and eventually evaporates. When there is graphene on top of the substrate, the melted substrate goes under the graphene lattice and hence causing its surface to elevate. Furthermore, the melted SiO₂ tends to move out from the edges of the hole causing the graphene to stretch out at the center and eventually break due to the strain under the pulsed-laser irradiation. Currie *et al.* have also reported such a behaviour of carbon bonds under the pulsed laser irradiation [18]. Fig. 4.36 shows a schematic representation of our explanation of the irradiation process.

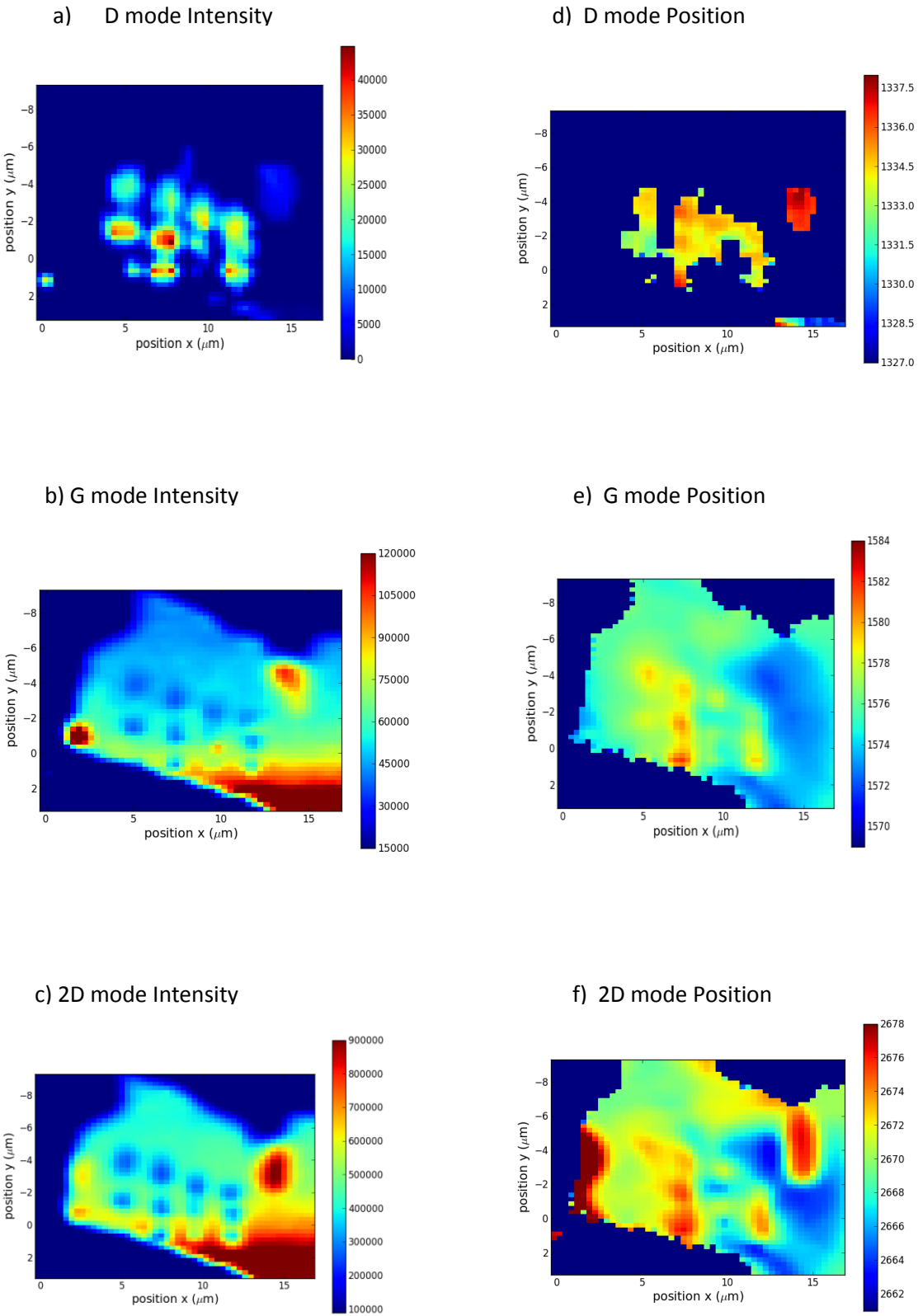
This process also suggests that the melted SiO₂ is attached to the graphene lattice and as a result doping is expected to occur which is approved by the G and 2D band upshifts in the Raman mapping images. Fig.4.35 (a)-(i) shows the Raman images of the investigated sample. Here, we have the peak intensities, peak positions and line widths of the D, G, and 2D bands. The D band intensity has increased at the modified regions which suggests that the defects are formed. These defects might be a result of graphene's lattice break, elevated surface, and lattice distortion.

The position of the D mode is almost the same over the whole modified region and can be estimated from the Raman image (Fig. 4.35 (d)) to be 1335 cm⁻¹. The line width of the D mode varies between 27 cm⁻¹ and 32 cm⁻¹.

The G mode intensity has decreased approximately by half. This is consistent with our assumptions such that the decrease in the amount of sp² bonded carbon atoms leads to the decrease in the G mode intensity. The upshift of the G mode can be interpreted as an evidence of doping. The G peak position in the unmodified region is about 1673 cm⁻¹ whereas on the modified region it shifts up to 1681 cm⁻¹ (by ~8 cm⁻¹). The line width of the G peak has slightly increased by 3 cm⁻¹ from about 12 cm⁻¹ to about 15 cm⁻¹.

2D mode intensity has distinctively decreased as a result of pulsed-laser irradiation. This result is not very surprising since the defects cause the 2D mode intensity decrease. The position of the 2D peak exhibits an upshift up to ~9 cm⁻¹ from ~2666 cm⁻¹ up to ~2675 cm⁻¹. Considering the upshift of G and 2D modes together we can conclude that the hole doping has occurred during the process [49]. The hole doping might be caused by the interaction with the

substrate and oxygen. The broadening of the 2D mode is also consistent with our explanation since disorder causes the broadening of all peaks [47].



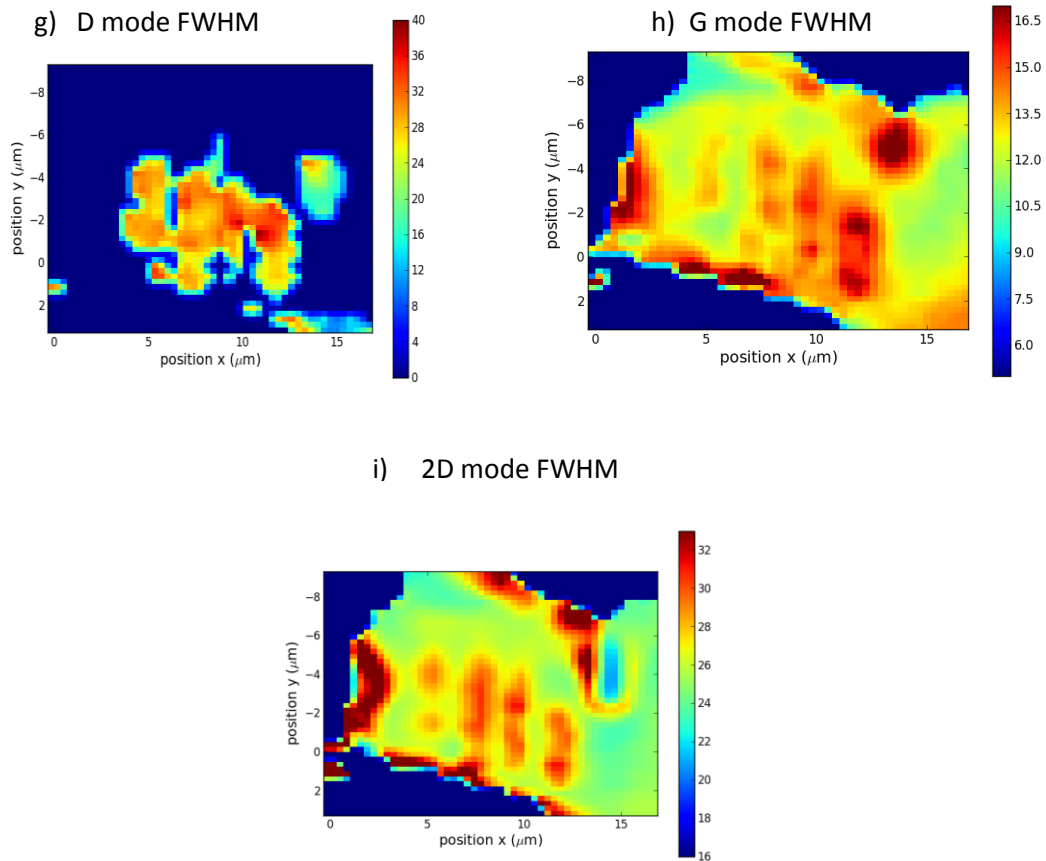


Fig. 4.35. The Raman images obtained after the pulsed laser irradiation of SLG. a) Intensity map of the D mode b) Intensity map of the G mode c) Intensity map of the 2D mode d) Position map of the D mode e) Position map of the G mode f) Position map of the 2D mode g) FWHM map of the D mode h) FWHM map of the G mode i) FWHM map of the 2D mode. The spatial resolution of the Raman maps is 400 nm. The Raman images are based on the peak-fitted parameters.

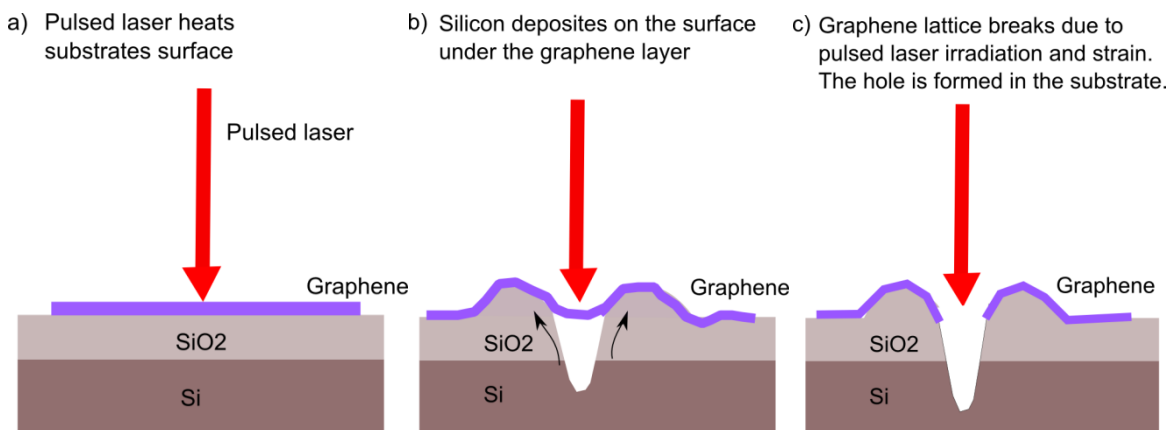


Fig. 4.36. The scheme showing the mechanism for the hole formation induced by pulsed laser irradiation of graphene on Si/SiO₂ substrate.

Chapter 5

Conclusion and Outlook

In this work we employ micro-Raman spectroscopy and Atomic Force Microscopy to reveal the laser-induced effects on mechanically exfoliated single-layer graphene on Si/SiO₂ substrate. We irradiated our graphene samples for about 10 minutes in an ambient conditions by using a Nd:YAG visible laser with 532 nm wavelength and maximal power P_{laser} ranging from 32 mW to 40 mW.

Our experimental results show a clear evidence that several events take place as a consequence of exposure of monolayer graphene to the high power laser. One of those events is the chemical functionalization of the graphene crystal lattice, generated by photo-induced chemical reactions presumably involving surrounding oxygen and water molecules trapped between Si/SiO₂ substrate and graphene. Secondly, the dissociation of adhesive residues present on the graphene surface, as a result of laser-induced heating, leads to the generation of amorphous carbon and hydrogenation of graphene. A third event is the structural modification of the single crystalline layer of graphene into a nanocrystalline structure. We also show that the reactivity of the graphene can be locally enhanced with laser treatment. As it has been confirmed by the experiments, all of these effects occur as a consequence of laser irradiation. Due to the simultaneous and possibly counteracting processes it is difficult to identify and distinguish significant effects of each event and interpret the changes in the Raman spectra of graphene.

We have conducted time-dependent micro-Raman measurements in order to monitor the changes occurring during the laser radiation and understand the mechanism behind these changes. The full results of the time-dependent Raman measurements are shown in the previous section. These repeatable, time-dependent Raman data exhibit sharp and frequent changes suggesting step by step processes taking place during the laser irradiation. The unusual decrease and disappearance of the D mode at the final stage after its sharp-cut increase is one of the most interesting and puzzling results of this experiment. It refers to either a reversible defect formation or formation and gradual removal of a foreign material such as amorphous carbon generated by tape residues.

We have also obtained the Raman intensity, position and line width maps of the D, G, and 2D peaks after the laser treatment. Our main conclusions are based on the final Raman maps since these changes are the outcome of our experiment and represent the stable equilibrium condition.

Further analysis with AFM showed a definite modified regions with a diameter of 1.4 μm involving etched and elevated areas. These laser-induced affected regions were localized without damaging the surrounding graphene area indicating a potential tool for patterning graphene. The repeated AFM measurement approved that these affected regions are stable in time. However heating the sample in a heating plate at a moderate temperature of 200 $^{\circ}\text{C}$ for 5 minutes induced pronounced changes on the morphology of the laser-affected regions.

In this work we also investigated the effects that appear after the pulsed laser irradiation of monolayer graphene. Again we have performed the Raman mapping measurements and AFM measurements in order to characterize our sample. The damage of the pulsed laser is much stronger and easy to observe than the visible laser. The AFM images show a distinctive hole inside of the graphene layer as well as silicon substrate. We observe elevated ring-shaped regions around the holes which are around 25 nm high. We propose the following explanation for this observation. The high power pulsed laser induces severe temperature increase and therefore the substrate melts down and moves out of its surface to the interface between silicon and graphene. This process causes a pronounced elevation of graphene's surface whereas no height increase is observed on the bare substrate surface. Eventually the strain caused by surface elevation and pulsed laser radiation causes graphene lattice to break down and form holes. The Raman mapping data is also in good agreement with our explanation. The upshifts in the G and 2D modes indicate an hole doping which can be caused by the interaction with the substrate and oxygen under pulsed laser-enhanced conditions. Here again the damaged regions does not affect the surrounding graphene regions and can be seen as a potential patterning tool.

Further work is needed to understand the behavior of the carbon bonds and interaction between the substrate, graphene and surrounding air during and after the laser irradiation. It could be helpful to conduct the experiment in the vacuum condition to distinguish the influence of oxygen. Free-standing graphene would be another option as a sample. It should be noted here that, although we had a free-standing graphene sample transferred on a TEM grid, due to the laser sensitivity of the TEM grid itself, it was difficult to distinguish the

effects on the free-standing sample. Moreover, the TEM analysis would be a great tool to characterize the modifications induced by the laser.

Our results provide a clue about intentional localized defect formation on the surface of graphene to tune its properties and patterning graphene by laser-beam lithography. The results throw light on the interaction between the laser and graphene layer supported by SiO₂ and possibility to induce local chemical reactions under a controlled manner.

Chapter 6

Zusammenfassung

In dieser Arbeit verwenden wir die Micro-Raman Spektroskopie und Raster-Kraft-Mikroskopie, um die Laser-induzierten Wirkungen von mechanisch expandiertem Einschicht-Graphen auf Si/SiO₂-Substrate aufzuzeigen. Wir haben unsere Graphen-Proben für ca. 10 Minuten unter Umgebungsbedingungen durch die Verwendung eines Nd:YAG-Festkörperlaserbeschrifters mit einer Wellenlänge von 532 nm und einer maximalen Laserleistung von 32 mW bis 40 mW bestrahlt.

Unsere Versuchsergebnisse zeigen eindeutig, dass als Folge der Aussetzung von Einschicht-Graphen auf Hochleistungsleiser mehrere Vorgänge stattfinden. Einer dieser Vorgänge ist die chemische Funktionalisierung der Graphen-Kristallgitter, die durch photo-induzierte chemische Reaktionen erzeugt wurden. Diese haben vermutlich die umgebenden Sauerstoff- und Wasserstoffmoleküle eingeschlossen, die zwischen Si/SiO₂-Substrat und Graphen gefangen waren. Zweitens, führt die Dissoziation von Klebstoffrückständen auf der Graphen-Oberfläche, als Folge der Laser-induzierten Erwärmung, zur Entstehung von amorphem Kohlenstoff und zur Hydrierung von Graphen. Eine dritte Folge ist die strukturelle Änderung des Graphens, nämlich von einer kristallinen Einschicht- zu einer nanokristallinen Struktur. Wir zeigen auch, dass die Reaktivität des Graphens mit der Laserbehandlung lokal verstärkt werden kann. Wie die Experimente bestätigt haben, treten alle diese Effekte als Folge der Laserbestrahlung auf. Aufgrund der gleichzeitigen und möglicherweise gegenläufigen Vorgänge ist es schwer, erhebliche Auswirkungen jedes einzelnen Vorgangs zu erkennen und zu unterscheiden und die Veränderungen in dem Raman-Spektrum des Graphens zu interpretieren.

Wir haben zeitabhängige Mikro-Raman-Messungen durchgeführt, um Veränderungen während der Laserbestrahlung zu beobachten und die Mechanismen hinter diesen Veränderungen zu verstehen. Die vollständigen Ergebnisse der zeitabhängigen Raman-Messungen werden im vorhergehenden Abschnitt gezeigt. Diese wiederholbaren, zeitabhängigen Rama-Daten zeigen starke und häufige Veränderungen auf, die darauf hindeuten, dass während der Laserbestrahlung ein Schritt für Schritt Prozess abläuft. Die ungewöhnliche Abnahme und Wegfall des D-Mode in der Schlussphase nach dem deutlichen

Anstieg ist einer der interessantesten und rätselhaftesten Ergebnisse dieses Experiments. Es bezieht sich entweder auf eine reversible Fehlbildung oder eine Bildung und schrittweisen Abbau eines Fremdstoffs wie amorpher Kohlenstoff, das durch Klebstoffrückstände erzeugt wurde.

Wir haben auch die Raman-Intensität, Position und Linienbreite Raman-Maps der D-, G- und 2D-Spitzenwerte nach der Laserbehandlung gewonnen. Unsere wichtigsten Schlussfolgerungen basieren auf den letzten Raman-Maps, da diese Veränderungen das Ergebnis unseres Experiments sind und den stabilen Gleichgewichtszustand darstellen.

Weitere Analysen mit AFM haben deutlich veränderte Regionen mit einem Durchmesser von 1,4 μm gezeigt, die geätzte und erhöhte Bereiche einschließen. Diese Laser-induzierte Regionen wurden lokalisiert ohne den umgebenden Graphen-Bereich zu beschädigen, welches auf ein mögliches Mittel für die Graphen-Strukturierung hinweist. Die wiederholte AFM Messung bestätigt, dass diese betroffenen Regionen zeitstabil sind. Dennoch hat das Erhitzen der Proben in einer Heizplatte bei mittlerer Temperatur von 200 $^{\circ}\text{C}$ deutliche Veränderungen in der Morphologie der Laserbetroffenen Regionen hervorgebracht.

In dieser Arbeit haben wir auch die Auswirkungen, die nach der gepulsten Laserbestrahlung auf Einschicht-Graphene entstanden sind, untersucht. Für die Bestimmung der Proben haben wir erneut die Raman-Mapping-Messungen und AFM-Messungen durchgeführt. Die Beschädigung des gepulsten Lasers ist viel stärker und leichter zu beobachten als die des sichtbaren Lasers. Die AFM-Bilder zeigen ein markantes Loch im Inneren der Graphenschicht sowie Siliziumsubstrat. Wir konnten erhöhte ringförmige Bereiche um die Löcher herum beobachten, die ca. 25 nm hoch sind. Wir schlagen folgende Erklärung für diese Beobachtung vor. Der gepulste Hochleistungs führt zu einem starken Temperaturanstieg und damit schmilzt das Substrat ein und bewegt sich aus seiner Oberfläche heraus und gelangt an die Schnittstelle zwischen dem Silizium und dem Graphen. Dieser Prozess führt zu einer deutlichen Erhebung der Graphenoberfläche wohingegen auf der bloßen rauen Oberfläche keine Erhöhung mehr beobachtet wird. Schließlich könnte die Erhebung der Oberfläche zur Verformung geführt haben und die gepulste Laserstrahlung dazu, dass das Graphengitter zerbrochen ist und sich Löcher gebildet haben. Die Raman-Mapping-Daten stimmen mit unserer Erklärung überein. Das Hoch in den G- und 2D-Modes zeigt eine Loch-Dotierung auf, die durch die Wechselwirkung mit dem Substrat und Sauerstoff unter gepulsten lichtenergierten Bedingungen entstanden sein könnte. Auch hier wirken sich die

geschädigten Regionen nicht auf die umliegenden Graphen-Bereiche aus und kann als ein mögliches Strukturierungsmittel angesehen werden.

Unsere Ergebnisse geben einen Hinweis auf die bewusst lokalisierte Fehlbildung auf der Graphen-Oberfläche, um ihre Eigenschaften und die Graphen-Strukturierung durch Laserstrahlolithographie anzupassen. Die Ergebnisse geben Aufschluss über die Interaktion zwischen Laser und Graphenschicht, die von SiO₂ unterstützt wird, und über die Möglichkeit unter kontrollierten Bedingungen lokale chemische Reaktionen hervorzurufen.

Appendix A. Python script

Sample script for the D mode fitting

```
##

## Fitting tool for Raman-mappings

##

## Attention: Insert two integers in the first row in input-file (x-axis)

##

import time

e0 = time.time()

c0 = time.clock()

import os

import numpy as np

from lmfit import minimize, Parameters

## deleting old output files

for file in os.listdir(os.curdir):

    if file == 'fittingparameters_D.dat':

        os.remove('fittingparameters_D.dat')

## load input file

for file in os.listdir(os.curdir):

    if file[-4:] == '.txt':

        data = np.loadtxt(file)

        x = data[0][1:][855:]

## defining fitting model, initial values and boundaries for the parameter

def residual(params, x_val, y_val):

    CB = params['CB'].value
```

```

LB = params['LB'].value

area1 = params['area1'].value

fwhm1 = params['fwhm1'].value

freq1 = params['frequency1'].value

lorentz2 = CB + LB*x_val + (2*area1)/np.pi*(fwhm1/(4*(x_val - freq1)**2 + fwhm1 **2))

return (y_val-lorentz2)

params = Parameters()

params.add('CB',      value=1000.)

params.add('LB',      value=1.)

params.add('area1',   value=500000.,  min=0.)

params.add('fwhm1',   value=100.,    min=10.,  max=200.)

params.add('frequency1', value=1340.,  min=1300., max=1400.)

## empty list for output parameters

output = np.zeros((len(data)-1,6))

## fitting process

for i in range(1,len(data)):

    y = data[i][1:][855:]

    params['CB'].value = 1000.

    params['LB'].value = 1.

    params['area1'].value = 500000.

    params['fwhm1'].value = 100.

    params['frequency1'].value = 1340.

    out = minimize(residual, params, args=(x, y))

    output[i-1][0] = data[i][0]

    output[i-1][1] = params['CB'].value

```

```

output[i-1][2] = params['LB'].value

output[i-1][3] = params['area1'].value

output[i-1][4] = params['fwhm1'].value

output[i-1][5] = params['frequency1'].value

## writing output to file

np.savetxt('fittingparameters_D.dat', output ,fmt='% .1f', delimiter=' ',newline='\n')

## print computational time

elapsed_time = time.time() - e0

cpu_time = time.clock() - c0

print 'elapsed_time [s]', elapsed_time

print 'cpu_time [s]', cpu_time

```

Sample script for the Raman maps fitting

```

#!/usr/bin/env python

import numpy as np

from matplotlib.mlab import griddata

import matplotlib.pyplot as plt

from mpl_toolkits.axes_grid1 import make_axes_locatable

data = np.transpose(np.loadtxt('fittingparameters_1L_D.dat'))

X = data[1]

Y = data[0]

Z = data[6]

```

```

xi = np.linspace(min(X), max(X))

yi = np.linspace(min(Y), max(Y))

zi = griddata(X, Y, Z, xi, yi)

fig = plt.figure()

ax = fig.add_subplot(111)

## Contour plot

im = plt.imshow(zi, interpolation='nearest',
extent=(min(X),max(X),max(Y),min(Y)),cmap=plt.cm.get_cmap('jet'))

im.set_clim(1325,1345)

plt.colorbar(im)

ax.set_ylabel("position y ( $\mu\text{m}$ )", fontsize = 15)

ax.set_xlabel("position x ( $\mu\text{m}$ )", fontsize = 15)

plt.axes().set_aspect('equal', 'box-forced')

## Histogramm

##plt.hist(zi.flatten(), 256, range=(0,70000), fc='k', ec='k')

plt.show()

```


Acknowledgment

I would like to express my gratitude to my advisor Prof. Dr. Jannik Meyer for his guidance, great support and his new ideas throughout this study. I also want to thank him that he made it possible for me to work in collaboration with the group of Prof. Dr. Janina Maultzsch at Technical University of Berlin.

I am heartily thankful to Prof. Dr. Janina Maultzsch, for her interest in this work and kind guidance. Her wide knowledge, enthusiasm in research and guidance helped me a lot to accomplish this thesis. I am grateful to have the chance to work with such a wonderful team!

My special thanks would go to Felix Herziger for helping me out with my experimental runs and providing valuable insights on Raman Spectroscopy of graphene. I have always been provided with every bit of help that I could possibly require. I would really appreciate his invaluable help and friendship.

I also want to thank Emanuele Poliani for the AFM measurements and his interesting ideas,

Meinke Reinhard for the pulsed laser experiments,

Jan Laudenbach and Nils Scheuschner for useful discussions,

Franz Eder for his help in transferring graphene flakes,

Dr. Aytac Jafarzade for her great support during my study,

and last but not least, my parents and my friends for always being there when I need them.

Bibliography

- [1] K. S. Novoselov. *Two-dimensional gas of massless Dirac fermions in graphene*. Nature 438, pp. 197-200. 2005
- [2] A. H. Castro Neto and K. S. Novoselov. *New directions in science and technology: two-dimensional crystals*, Rep. Prog. Phys. 74, p. 082501, 2011
- [3] S. Chen. *Thermal conductivity of isotopically modified graphene*. Nature Matter. 11, 2012
- [4] J. Rafiee. *Wetting transparency of graphene*. Nature Matter 11, 2012
- [5] K. S. Novoselov, Z. Jiang, Y. Zhang, S. V. Morozov, H. L. Stormer, U. Zeitler, J. C. Maan, G. S. Boebinger, P. Kim, A. K. Geim. *Room-temperature Quantum Hall Effect in graphene*. Science 315, p. 1379. 2007.
- [6] M.I. Katsnelson. *Graphene: carbon in two dimensions*. Materials today 10, p. 20-27, 2007.
- [7] A. Pototsky, F. Marchesoni, F. V. Kusmartsey, P. Hanggi, and S. E. Savel'ev. *Relativistic Brownian motion in graphene chip*. European Physical Journal B 85, p. 356, 2012.
- [8] C. R. Dean, A. F. Young, P. Cadden-Zimansky, L. Wang, H. Ren, K. Watanabe, T. Taniguchi, P. Kim, J. Hone, and K. L. Shepard. *Multicomponent fractional quantum Hall effect in graphene*. Nature Phys. 7, p. 693-696. 2011.
- [9] K. I. Bolotin, K. J. Sikes, Z. Jiang, M. Klima, G. Fudenberg, J. Hone, P. Kim, H. L. Stormer. *Ultrahigh electron mobility in suspended graphene*. Solid State Communications 146. p. 351, 2008.
- [10] A. A. Balandin, S. Ghosh, W. Bao, I. Calizo, D. Teweldebrhan, F. Miao, and C. N. Lau. *Superior thermal conductivity of single-layer graphene*. Nano. Lett. 8 (3), 902-907, 2008.
- [11] C. Lee, X. Wei, J. W. Kysar, J. Hone. *Measurement of the elastic properties and intrinsic strength of monolayer graphene*. Science 321 (5887), 385-388. 2008.
- [12] A. K. Geim, K.S. Novoselov. *The rise of graphene*. Nature Materials 6, p183-191, 2007.
- [13] M. Xu, D. Fujita, N. Hanagata. *Monitoring electron-beam irradiation effects on graphenes by temporal Auger electron spectroscopy*. Nanotechnology 21, 265705, 2010.
- [14] A. Das, S. Pisana, B. Chakraborty, S. Piscanec, S. K. Saha, U. V. Waghmare, K. S. Novoselov, H. R. Krishnamurthy, A. K. Geim, A. C. Ferrari & A. K. Sood. *Monitoring dopants by Raman scattering in an electrochemically top-gated graphene transistor*. Nat. Nanotechnology, 3(4), 210-215, 2008.
- [15] A. V. Krashennikov, and F. Bahnhart. *Engineering of nanostructured carbon materials with electron or ion beams*. Nature Materials 6, 723-733, 2007.

- [16] M. M. Lucchese, F. Stavale, E. H. Martins Ferreira, C. Vilani, M. V. O. Moutinho, R. B. Capaz, C. A. Achete, and A. Jorio. *Quantifying ion-induced defects and Raman relaxation length in graphene*. Carbon, 48(5), pp. 1592-1597, 2010.
- [17] B. Krauss, T. Lohmann, D. H. Chae, M. Haluska, K von Klitzing, and J.H. Smet. *Laser-induced disassembly of a graphene single crystal into a nanocrystalline network*. Phys. Rev. B 79, 165428, 2009
- [18] M. Currie, J. D. Caldwell, F. J. Bezares, J. Robinson, T. Anderson, H. Chun, and M. Tadjer. *Quantifying pulsed laser induced damage to graphene*. App. Phys. Lett. 99, 211909, 2011.
- [19] H. Liu, S. Ryu, Z. Chen, M. L. Steigerwald, C. Nuckolls, and L. E. Brus. *Photochemical reactivity of Graphene*. J. Am. Chem. Soc. Vol. 131, No:47, 2009.
- [20] K. S. Novoselov, A. K. Geim, S. V. Morozov, D. Jiang, Y. Zhang, *et al.*, *Electric Field Effect in Atomically Thin Carbon Films*. Science 306, 666 – 669, 2004.
- [21] L. D. Landau and E. M. Lifshitz. *Statistical Physics Part I*. Pergamon Oxford, 1980
- [22] N. D. Mermin. *Crystalline order in two dimensions*. Phys. Rev. 176, 250-254. 1968
- [23] J. C. Meyer, A.K. Geim, M.I. Katsnelson, K.S Novoselov, T.J. Booth, S. Roth. *The structure of suspended graphene sheets*. Nature 446, 60–63, 2007.
- [24] F. Herziger. *Raman spectroscopy of perturbations in graphene*. Master thesis, TU Berlin, 2012
- [25] B. T. Kelly. *Physics of Graphite*. Applied Science: London, 1981.
- [26] M. S. Dresselhaus, G Dresselhaus, P. C. Eklund. *Science of Fullerenes and Carbon Nanotubes*. Academic Press. San Diego, CA, p 965, 1995.
- [27]] A. H. Castro Neto, F. Guinea, N. M. R. Peres, K. S. Novoselov, and A. K. Geim. *The electronic properties of graphene*. Rev. Mod. Phys., vol. 81, no. 1, pp. 109–162, 2009.
- [28] I. W. Frank, D. M. Tanenbaum, A. M. van der Zande and P. L. McEuen, J. Vac. *Mechanical properties of suspended graphene sheets*. Sci. Technol. B, 25, 2558-2561, 2007
- [29] M. C. Lemme. *Current status of graphene transistors*. Solid State Phenom. 156-158, 499-509, 2009.
- [30] P. R. Wallace. *The Band Theory of Graphite*. Physical Review 71, 622 – 634 , 1947.
- [31] R. Saito, G. Dresselhaus, and M. S. Dresselhaus, *Physical Properties of Carbon Nanotubes*. Imperial, London, 1998.

- [32] S. Reich, J. Maultzsch, C. Thomsen, and P. Ordejon. *Tight-binding description of graphene*, Physical Review B 66, 035 412, 2002.
- [33] M.S. Purewal, Y. Zhang, and P. Kim. *Unusual transport properties in carbon based nanostructured materials: nanotubes and graphene*. Physica Status Solidi (B), vol. 243, pp. 3418-3422, 2006.
- [34] C. Kittel. *Introduction to solid state physics*. Wiley, 1996.
- [35] M. S. Dresselhaus, A. Jorio and R. Saito. *Characterizing graphene, graphite, and carbon nanotubes by Raman spectroscopy*. Annu. Rev. Condens. Mat. Phys. 1, p.89-108, 2010
- [36] J. Maultzsch, S. Reich, C. Thomsen, H. Requard, and P. Ordejon. *Phonon dispersion in graphite*. Phys. Rev. Lett., 92:75501, 2004.
- [37] L. M. Malard, M. A. Pimenta, G. Dresselhaus, and M. S. Dresselhaus. *Raman spectroscopy in graphene*. Physics Reports, 473(5-6), 51-87, 2009.
- [38] M. Mohr, J. Maultzsch, E. Dobardzcaronicacute, S. Reich, I. Miloscaronevicacute, M. Damnjanovicacute, A. Bosak, M. Krisch, C. Thomsen. *Phonon dispersion of graphite by inelastic x-ray scattering*. Phys. Rev. B, 76, 035439, 2007.
- [39] A. C. Ferrari and J. Robertson. *Interpretation of Raman spectra of disordered and amorphous carbon*. Physical Review B, 61(20), 14095-14107, 2000.
- [40] W. Kohn. *Image of the Fermi Surface in the Vibration Spectrum of a Metal*. Physical Review Letters, 2(9), 393-394, 1959.
- [41] C. V. Raman, K. S. Krishnan. *A new type of secondary radiation*. Nature 121, 501 1928.
- [42] *The Nobel Prize in Physics 1930*. Taken from: http://www.nobelprize.org/nobel_prizes/physics/laureates/1930/. (cited 14 July 2013)
- [43] S. Reich, C. Thomsen, and J. Maultzsch, *Carbon Nanotubes: Basic Concepts and Physical Properties*. Wiley-VCH, 2004.
- [44] D. J. Ingle, R. S. Crouch, *Spectrochemical Analysis*. Prentice-Hall, Inc. Upper Saddle River, NJ, 1988.
- [45] P. Larkin. *Infrared and Raman Spectroscopy; Principles and Spectral Interpretation*. Elsevier, 2011.
- [46] E. Smith and G. Dent. *Modern Raman Spectroscopy-A Practical Approach*. John Wiley & Sons, Inc., England, 2005.

- [47] A. C. Ferrari. *Raman spectroscopy of graphene and graphite: Disorder, electron–phonon coupling, doping and nonadiabatic effects*. Solid State Communications, Volume 143, p .47-57, 2007.
- [48] A. Eckmann, A. Felten, A. Mishchenko, L. Britnell, R. Krupke, K.S. Novoselov, C. Casiraghi. *Probing the Nature of Defects in Graphene by Raman Spectroscopy*. Nano Lett. 12, 3925–3930, 2012.
- [49] A. Das, S. Pisana, B. Chakraborty, S. Piscanec, S. K. Saha, U. V. Waghmare, K. S. Novoselov, H. R. Krishnamurthy, A. K. Geim, A. C. Ferrari & A. K. Sood. *Monitoring dopants by Raman scattering in an electrochemically top-gated graphene transistor*. Nat. Nanotechnology, 3(4), 210-215, 2008.
- [50] M. S. Dresselhaus, A. Jorio, M. Hofmann, G. Dresselhaus, and R. Saito. *"Perspectives on Carbon Nanotubes and Graphene Raman Spectroscopy"*, Nano Letters 10, pp. 751-758, 2010.
- [51] Y. Y. Wang, Z. H. Ni, Z. X. Shen, H. M. Wang, and Y. H. Wu. *Interference enhancement of Raman signal of graphene*. Applied Physics Letters, vol. 92, no. 4, 043121, 2008.
- [52] R. J. Nemanich and S. A. Solin. *First and second-order Raman scattering from finite-size crystals of graphite*. Physical Review B, 20(2), 1979.
- [53] C. Casiragi, S. Pisana, K.S. Novoselov, A.K. Geim, A.C. Ferrari. *Raman Fingerprint of Charged Impurities in Graphene*. App. Phys. Lett. 91, 233108, 2007
- [54] C. Thomsen and S. Reich. *Double resonant Raman scattering in graphite*. Physical Review Letters **85**, 5214 – 5217, 2000.
- [55] J. Maultzsch. *Vibrational properties of carbon nanotubes and graphite*. PhD thesis, 2004.
- [56] J. Jiang, R. Saito, A. Grüneis, S.G. Chou, G.G. Samsonidze, A. Jorio, G. Dresselhaus, and M.S. Dresselhaus. *Photoexcited electron relaxation processes in single wall carbon nanotubes*. Phys. Rev. B 71, pp. 45417–45419, 2005.
- [57] L. G. Cançado, A. Jorio, E. H. Martins Ferreira, F. Stavale, C. A. Achete, R. B. Capaz, M. V. O. Moutinho, A. Lombardo, T. S. Kulmala, and A. C. Ferrari. *Quantifying Defects in Graphene via Raman Spectroscopy at Different Excitation Energies*, Nano Letters. 11 (8), 3190-3196 , 2011
- [58] F. Tunistra and J.L Koenig. *Raman Spectrum of Graphene*. J. Chem. Phys.,53, pp. 1126–1130, 1970.

- [59] M. M. Lucchese, F. Stavale, E. H. Martins Ferreira, C. Vilani, M. V. O. Moutinho, R. B. Capaz, C. A. Achete, and A. Jorio. *Quantifying ion-induced defects and Raman relaxation length in graphene*. Carbon, 48(5), pp. 1592-1597, 2010.
- [60] A. C. Ferrari, and J. Robertson, *Raman Spectroscopy of amorphous, nanostructured, diamond-like carbon, and nanodiamond*. Phil. Trans. Royal. Soc. A 362, 2477, 2004
- [61] B. Guo, L. Fang, B. Zhang, J. R. Gong. *Graphene Doping: A Review*. Insciences Journal, 1(2), 80-89, 2011.
- [62] A. C. Ferrari, J. C. Meyer, V. Scardaci, C. Casiraghi, M. Lazzeri, F. Mauri, P. Piscanec, D. Jiang, K. S. Novoselov, S. Roth and A. K. Geim. *Raman spectroscopy of graphene and few layers graphene*. Phys. Rev. Lett. 97, 18740-1, 2006.
- [63] J. C. Meyer, C. O. Girit, M. F. Crommie, and A. Zettl. *Hydrocarbon lithography on graphene membranes*. App. Phys. Letters. 92 (123110) , 2008.
- [64] D. M. Basko, S. Picanes, A.C. Ferrari. *Electron-electron interactions and doping dependence of the two-phonon Raman intensity in graphene*. Phys. Rev. B, 80, 165413-165422, 2009.
- [65] M. Hulmann, M. Haluska, G. Scalia, D. Obergfell, and S. Roth. *Effects of charge impurities and laser energy of Raman spectra of graphene*. Nano Lett. 8, 3594, 2008.
- [66] J. Hong, M. K. Park, E. J. Lee, D. E. Lee, D. S. Hwang and S. Ryu. *Origin of new broad Raman D and G peaks in annealed graphene*. Scientific Reports, 3:2700, DOI: 10.1038, srep02700, 2013.
- [67] J. Song, T. Y. Ko, and S. Ryu. *Raman spectroscopy study of annealing-induced effects on graphene prepared by micromechanical exfoliation*. Bull Korean Chem Soc. 31, 2679, 2010.
- [68] Y. Y. Wang, Z. H. Ni, T. Yu, Z. X. Shen, H. M. Wang, Y. H. Wu, W. Chen, and A. T. Wee. *Raman studies of Monolayer Graphene: The substrate effect*. J. Phys. Chem. C, vol. 112, no. 29, 2008
- [69] P. N. Incze, G. Magda, K. Kamaras, and L. P. Biro. *Crystallographically selective nanopatterning of graphene on SiO₂*. Nano Res. 3, 110-116, 2010.
- [70] G. Ahn, H. R. Kim, B. H. Hong and S. Ryu. *Raman spectroscopy study on the reactions of UV-generated oxygen atoms with single-layer graphene on SiO₂/Si substrates*. Carbon Letters Vol. 13, No:1, 34-38, 2012.
- [71] Carbon Black. taken from: <https://graphene-supermarket.com/Carbon-Black.html>(cited on 17.12.2013)

- [72] S. Stankovich, D. A. Dikin, R. D. Piner, K. A. Kohlhaas, A. Kleinhammes, Y. Jia, Y. Wu, S. T. Nguyen, R. S. Ruoff. *Synthesis of graphene-based nanosheets via chemical reduction of exfoliated graphite oxide*. Carbon, No: 45, 2007.
- [73] N. Mitoma, R. Nouchi, and K. Tanigaki. *Photo-oxidation of Graphene in the Presence of Water*. The journal of Physical Chemistry, C 117, 73-220, 2013.
- [74] M. Wall. *The Raman Spectroscopy of Graphene and the Determination of Layer thickness*. Thermo Fisher Scientific, 2011.
- [75] M. Ishigami, J.H. Chen, W. G. Cullen, M. S. Fuhrer, and E. D. Williams. *Atomic structure of graphene on SiO₂*. Nano Lett. 7, 1643, 2007.

Curriculum Vitae

Rasim Mirzayev

Education

1995-2000: Agdash Private Science Lyceum , Agdash / Azerbaijan

2000-2008: Bogazichi University, Istanbul / Turkey

“Integrated bachelors and masters program in teaching physics”

2004-2005: Scotts College London, Advanced English Course, London/ UK

2011-2014: Vienna University , Vienna/Austria

Master study in Physics

Language Skills

Azerbaijani - native

Turkish - native

German - intermediate

English - advanced

Russian - advanced

Computer Skills

Good skills in Microsoft Word, Excel, Powerpoint, Adobe Photoshop, and Html.